



Coagulation Instability in Protoplanetary Disks: A Novel Mechanism Connecting Collisional Growth and Hydrodynamical Clumping of Dust Particles

Ryosuke T. Tominaga^{1,2} , Shu-ichiro Inutsuka¹ , and Hiroshi Kobayashi¹

¹ Department of Physics, Nagoya University, Nagoya, Aichi 464-8692, Japan; rttominaga@nagoya-u.jp, ryosuke.tominaga@riken.jp

² RIKEN Cluster for Pioneering Research, 2-1 Hirosawa, Wako, Saitama 351-0198, Japan

Received 2020 December 4; revised 2021 July 6; accepted 2021 July 21; published 2021 December 8

Abstract

We present a new instability driven by a combination of coagulation and radial drift of dust particles. We refer to this instability as “coagulation instability” and regard it as a promising mechanism to concentrate dust particles and assist planetesimal formation in the very early stages of disk evolution. Because of dust-density dependence of collisional coagulation efficiency, dust particles efficiently (inefficiently) grow in a region of positive (negative) dust density perturbations, leading to a small radial variation of dust sizes and as a result radial velocity perturbations. The resultant velocity perturbations lead to dust concentration and amplify dust density perturbations. This positive feedback makes a disk unstable. The growth timescale of coagulation instability is a few tens of orbital periods even when dust-to-gas mass ratio is on the order of 10^{-3} . In a protoplanetary disk, radial drift and coagulation of dust particles tend to result in dust depletion. The present instability locally concentrates dust particles even in such a dust-depleted region. The resulting concentration provides preferable sites for dust–gas instabilities to develop, which leads to further concentration. Dust diffusion and aerodynamical feedback tend to stabilize short-wavelength modes, but do not completely suppress the growth of coagulation instability. Therefore, coagulation instability is expected to play an important role in setting up the next stage for other instabilities, such as streaming instability or secular gravitational instability, to further develop toward planetesimal formation.

Unified Astronomy Thesaurus concepts: [Protoplanetary disks \(1300\)](#); [Hydrodynamics \(1963\)](#); [Planetesimals \(1259\)](#)

1. Introduction

Formation of kilometer-sized planetesimals is an important step during growth from dust grains to planets in protoplanetary disks. Formation mechanisms are still under debate because of some barriers against dust growth. One of the barriers is the “radial drift barrier.” Dust particles are subject to significant radial drift toward a central star as a result of aerodynamical interaction with gas once they grow into intermediate-sized grains (Weidenschilling 1977; Nakagawa et al. 1986). The sizes of those grains are on the order of centimeters to meters in minimum-mass solar nebula (MMSN; Hayashi 1981). Fast radial drift generally prevents further dust growth, although it depends on disk models including an initial dust-to-gas mass ratio (Brauer et al. 2008).

Several mechanisms have been proposed to explain the origin of planetesimals. Okuzumi et al. (2012) showed that collisional growth of fluffy dust aggregates can overcome the drift barrier and forms planetesimals in an inner disk region. Resultant fluffy aggregates are compressed by both surrounding gas and self-gravity of aggregates toward kilometer-sized planetesimals with a density of 0.1 g cm^{-3} (Kataoka et al. 2013a, 2013b).

Hydrodynamical instabilities are also possible mechanisms of planetesimal formation. Hydrodynamical processes may be more important to form outer planetesimals and larger bodies than direct coagulation because coagulation takes longer time at outer radii. Streaming instability is one possible instability to assist planetesimal formation (Youdin & Goodman 2005; Youdin & Johansen 2007; Jacquet et al. 2011). The streaming instability can lead to dust clumping, and resultant clumps eventually collapse self-gravitationally once those mass densities exceed

Roche density (e.g., Johansen et al. 2007; Simon et al. 2016). The validity of streaming instability depends on the dust-to-gas mass ratio and dimensionless stopping time $\tau_s \equiv t_{\text{stop}}\Omega$, where Ω is the orbital frequency of a disk (e.g., Johansen et al. 2009b; Carrera et al. 2015; Yang et al. 2017). Carrera et al. (2015) and Yang et al. (2017) numerically investigated conditions for streaming instability to result in the strong dust clumping required for subsequent gravitational collapse. They showed that the dust-to-gas mass ratio should be larger than 0.02 for dust of $\tau_s = 0.1$, and higher dust abundance is necessary for smaller dust ($\tau_s = 10^{-2} - 10^{-3}$). In the presence of turbulent diffusion of dust particles, strong clumping via streaming instability requires much higher dust abundance (Chen & Lin 2020; Gole et al. 2020; Umurhan et al. 2020). The global gas pressure profile also affects the critical dust-to-gas mass ratio, and a small radial pressure gradient is preferable for strong clumping (e.g., Bai & Stone 2010; Abod et al. 2019; Gerbig et al. 2020).

Secular gravitational instability (GI) is also a possible mechanism leading to planetesimal formation (Ward 2000; Youdin 2011; Takahashi & Inutsuka 2014). The instability can develop even in self-gravitationally stable disks and create multiple dust rings that will azimuthally fragment (Tominaga et al. 2018, 2020). Linear analyses based on two-fluid equations show that secular GI requires high dust-to-gas mass ratio, as in the case of streaming instability. The required dust-to-gas mass ratio is larger than 0.02 for $\tau_s = 0.1$ in weakly turbulent disks (see Figure 11 in Tominaga et al. 2019). Tominaga et al. (2019) presented another secular instability called two-component viscous GI (TVGI). Although TVGI is operational in relatively dust-poor disks where secular GI cannot operate, a high dust-to-gas ratio (>0.02) seems to be required for TVGI to develop within hundreds of orbits.

As mentioned above, the hydrodynamical instabilities require large dust particles ($\tau_s \sim 0.1$) with an abundance higher than the usually assumed value of 0.01. However, according to numerical studies of dust coagulation, dust surface density significantly decreases as dust grows into sizes of $\tau_s \sim 0.1$ (e.g., Brauer et al. 2008; Okuzumi et al. 2012). Although fragmentation replenishes dust that avoids significant radial drift if its critical velocity is very low (a few m/s; Birnstiel et al. 2009), it may be inefficient to trigger the above instabilities because those fragments have not only low τ_s but also depleted to some extent. Therefore, for the above dust–gas instabilities to operate, dust particles have to avoid the depletion and accumulate via other mechanisms in advance unless solid materials are supplied from a surrounding envelope.

Pressure bumps and zonal flows in gas disks are possible sites of dust concentration (e.g., Whipple 1972; Kretke & Lin 2007; Johansen et al. 2009a; Dzyurkevich et al. 2010; Bai & Stone 2014; Flock et al. 2015). Streaming instability in pressure bumps has been investigated both analytically (Auffinger & Laibe 2018) and numerically (Taki et al. 2016; Carrera et al. 2021). Auffinger & Laibe (2018) and Carrera et al. (2021) showed that streaming instability develops for a dust-to-gas ratio of 0.01 if the relative amplitude of a pressure bump is larger than 10%–20%. We should note that deformation of a bump via frictional backreaction potentially inhibits subsequent gravitational collapse (Taki et al. 2016). Vortices also trap dust particles (e.g., Barge & Sommeria 1995; Chavanis 2000; Lyra & Lin 2013; Raettig et al. 2015), and observed lopsided structures in disks can be explained by such a dust-trapping mechanism (e.g., Fukagawa et al. 2013; van der Marel et al. 2013; Casassus et al. 2015).

Solid concentration can also occur near the water snow line (e.g., Stevenson & Lunine 1988; Dr azkowska & Dullemond 2014; Dr azkowska & Alibert 2017; Schoonenberg & Ormel 2017; Schoonenberg et al. 2018). Water ice evaporates when it passes the snow line. Release of fragile silicate can result in traffic jam and solid enhancement inside the snow line. For the traffic jam to operate, fragmentation of silicate whose critical velocity is \sim a few m/s (Dr azkowska & Alibert 2017) or disintegration of aggregates and the release of small silicate cores (Saito & Sirono 2011) is required. At the same time, the water vapor diffuses outward and recondenses onto icy solids, which increases solid abundance outside the snow line. Schoonenberg & Ormel (2017) showed that the solid enhancement outside the snow line is more efficient. Besides, recent experiments suggest that dry silicate grains are less fragile than previously considered (Kimura et al. 2015; Steinpilz et al. 2019), which might make the solid enhancement inside the snow line inefficient.

In this work, we present a new instability that can be another promising mechanism to accumulate dust particles that are subject to depletion via radial drift. The new instability, which we refer to as “coagulation instability,” is triggered by dust coagulation, which is completely distinct from the other dust–gas instabilities previously studied. Coagulation instability is distinct from the self-induced dust traps proposed by Gonzalez et al. (2017). The present instability does not require backreaction to gas, as shown in Section 2, whereas the latter mechanism does require the backreaction. We show that coagulation instability operates even when dust abundance decreases down to the order of 10^{-3} . In the new mechanism, dust particles actively play a role in concentrating themselves,

in contrast to mechanisms involving pressure bumps, zonal flow, and vortices.

This paper is organized as follows. Section 2 gives physical understanding of coagulation instability based on one-fluid linear analyses. In Section 3, we perform more comprehensive linear analyses based on both dust and gas equations. Although we only consider turbulence-driven coagulation in diffusion-free disks in Sections 2 and 3, we discuss effects of dust diffusion and other components of relative velocities in Sections 4.1 and 4.3. In Section 4.2, we discuss how the drag feedback (backreaction) at the midplane affects coagulation instability. We also compare the growth timescale and the traveling time of perturbations in Section 4.4. Section 4.5 discusses the effects of fragmentation. Section 4.6 gives speculation on coevolution with other dust–gas instabilities. We conclude in Section 5.

2. Simplified Analyses for Physical Understanding

We first give the physical interpretation of the coagulation instability based on simplified linear analyses. Analyses presented here only consider the motion of dust in a steady gas disk. This one-fluid analysis provides clear understanding of the coagulation instability.

2.1. Basic Equations

We describe dust motion using the vertically integrated continuity equation. In the Cartesian local shearing sheet (Goldreich & Lynden-Bell 1965) whose radial distance r from a star is R and Keplerian orbital frequency is Ω , the dust continuity equations is

$$\frac{\partial \Sigma_d}{\partial t} + \frac{\partial \Sigma_d v_x}{\partial x} = 0, \quad (1)$$

where x and v_x are the radial coordinate and velocity, respectively. The radial velocity of the dust is given by the terminal drift velocity (Adachi et al. 1976; Nakagawa et al. 1986):

$$v_x = -\frac{2\tau_s}{1 + \tau_s^2} \eta R \Omega, \quad (2)$$

where η is given as a function of radial distance r and gas density ρ_g :

$$\eta \equiv -\frac{1}{2\rho_g r \Omega^2} \frac{\partial c_s^2 \rho_g}{\partial r}, \quad (3)$$

where c_s is the sound speed. Another important physical value in the dust dynamics is Stokes number $\text{St} \equiv t_{\text{stop}}/t_{\text{eddy}}$, where t_{eddy} is the turnover time of the largest eddy. Hereafter, considering cases of $t_{\text{eddy}} = \Omega^{-1}$, we assume $\tau_s = \text{St}$.

Dust coagulation is described by the Smoluchowski equation for column number density of dust per unit particle mass m (e.g., Smoluchowski 1916; Schumann 1940; Safronov 1972; Brauer et al. 2008; Birnstiel et al. 2012; Okuzumi et al. 2012). Since analytical approaches of such a coagulation equation are difficult, we use a moment equation describing the size evolution of dust particles that dominate the total dust mass (see Estrada & Cuzzi 2008; Ormel & Spaans 2008; Sato et al. 2016). The mass of such dust particles is called the peak mass (Ormel & Spaans 2008), which is denoted by m_p in the

following. The time evolution of m_p is governed by

$$\frac{dm_p}{dt} = \frac{2\sqrt{\pi}a^2\Delta v_{pp}}{H_d}\Sigma_d, \quad (4)$$

where a is the particle radius, Δv_{pp} is the particle–particle collision velocity, and H_d is the dust scale height (see Sato et al. 2016). In this work, we only consider spherical dust particles, and m_p is thus given by $m_p = 4\pi\rho_{\text{int}}a^3/3$, where ρ_{int} is the internal mass density of a dust particle. In addition, our analyses focus on small particles that are in the Epstein regime

$$\tau_s = \sqrt{\frac{\pi}{8}} \frac{\rho_{\text{int}}a}{\rho_g c_s} \Omega. \quad (5)$$

If one assumes the vertically Gaussian profile of the gas density

$$\rho_g(z) = \frac{\Sigma_g}{\sqrt{2\pi}H} \exp\left(-\frac{z^2}{2H^2}\right), \quad (6)$$

where $H \equiv c_s/\Omega$ is the gas scale height, the normalized stopping time at the midplane can be written in terms of the gas surface density Σ_g :

$$\tau_s = \frac{\pi}{2} \frac{\rho_{\text{int}}a}{\Sigma_g}. \quad (7)$$

Although τ_s varies in the vertical direction, we use the midplane value of τ_s to refer the representative dust size in our vertically integrated formalism because most of the mass resides around the midplane. The simplified analyses given in this section assume the gas surface density to be constant: $\Sigma_g = \Sigma_{g,0}$. In such a case, Equations (4) and (7) give the evolutionary equation of τ_s :

$$\frac{\partial\tau_s}{\partial t} + v_x \frac{\partial\tau_s}{\partial x} = \frac{\sqrt{\pi}}{4} \left(\frac{\Sigma_d}{\Sigma_{g,0}}\right) \left(\frac{\Delta v_{pp}}{\tau_s H_d}\right) \tau_s. \quad (8)$$

Giving a specific expression of Δv_{pp} closes the set of the equations. In Sections 2 and 3, we focus on the turbulence-induced collisions. Although the turbulence-induced velocity generally depends on Reynolds number and eddy classes (Völk et al. 1980), we use the simplified expression $\Delta v_{pp} = \sqrt{C\tau_s}\alpha c_s$ valid for intermediate-sized dust particles (Ormel & Cuzzi 2007), where C is a numerical factor and α is the strength of turbulence (Shakura & Sunyaev 1973). The simplified expression allows us to easily perform further analyses. Sato et al. (2016) effectively considered a size dispersion by introducing a size ratio to calculate Δv_{pp} . They showed that Equation (4) with the size ratio of 0.5 well-reproduces the peak-mass evolution obtained from simulations with a size distribution. We thus follow their formalism. In such a case, the numerical factor C is about 2.3 (see Equation (28) in Ormel & Cuzzi 2007). We also use the simplified expression for the dust scale height to proceed analytical discussions: $H_d = \sqrt{\alpha/\tau_s}H$ (Dubrulle et al. 1995; Carballido et al. 2006; Youdin & Lithwick 2007). These simplifications give the following equation for τ_s :

$$\frac{\partial\tau_s}{\partial t} + v_x \frac{\partial\tau_s}{\partial x} = \frac{\Sigma_d}{\Sigma_{g,0}} \frac{\tau_s}{3t_0}, \quad (9)$$

where $t_0 \equiv (4/3\sqrt{C\pi})\Omega^{-1} \simeq 0.49\Omega^{-1}$ is mass growth time of a dust particle. Equations (1) and (9) are the governing equations in the simplified analyses.

Note that the coagulation rate $m_p^{-1}\partial m_p/\partial t \propto \tau_s^{-1}\partial\tau_s/\partial t$ is independent from the value of α because the following two processes are canceled out: (1) stronger turbulence stirs dust grains up more and increases $H_d \propto \alpha^{1/2}$, and thus the midplane dust density decreases with α ; (2) in contrast, the dust-to-dust collision velocity Δv_{pp} increases with α ($\Delta v_{pp} \propto \alpha^{1/2}$). As a consequence, the coagulation rate is determined by the dust-to-gas surface density ratio as already mentioned in previous studies (e.g., Brauer et al. 2008; Okuzumi et al. 2012). More specifically, the rate is related to the “total” gas surface density Σ_g ($\Sigma_{g,0}$), not a gas density averaged within a dust sublayer. This is also the case if turbulence is too weak and the settling velocity determines the collision rate (see Nakagawa et al. 1981).

2.2. Linear Analyses

We first construct the unperturbed state. For simplicity, we ignore the evolution of the background state via coagulation, and assume uniform surface density $\Sigma_{d,0}$ with a uniform dimensionless stopping time $\tau_{s,0}$ and the velocity $v_{x,0} = -2\tau_{s,0}\eta R\Omega/(1 + \tau_{s,0}^2)$. This assumption is valid if the instability is faster than coagulation. As shown below, coagulation instability satisfies this condition at wavelengths shorter than $3t_0|v_{x,0}|/\varepsilon$, where $\varepsilon \equiv \Sigma_{d,0}/\Sigma_{g,0}$ is the unperturbed dust-to-gas surface density ratio.

2.2.1. Dispersion Relation

Based on the above unperturbed state, we obtain the following linearized equations from Equations (1), (2), and (9):

$$(n + ikv_{x,0})\delta\Sigma_d + ik\Sigma_{d,0}\delta v_x = 0, \quad (10)$$

$$\delta v_x = \frac{1 - \tau_{s,0}^2}{1 + \tau_{s,0}^2} \frac{\delta\tau_s}{\tau_{s,0}} v_{x,0}, \quad (11)$$

$$(n + ikv_{x,0})\delta\tau_s = \frac{\delta\Sigma_d}{\Sigma_{g,0}} \frac{\tau_{s,0}}{3t_0} + \frac{\Sigma_{d,0}}{\Sigma_{g,0}} \frac{\delta\tau_s}{3t_0}, \quad (12)$$

where n and k are the complex growth rate and the wavenumber of perturbations, and we assume the exponential form of perturbations, i.e., $\delta\Sigma_d \propto \delta v_x \propto \delta\tau_s \propto \exp(ikx + nt)$. The wave-like perturbation on τ_s represents fast or slow coagulation (see Figure 1). The negative $\delta\tau_s$ means not fragmentation but “delayed” coagulation compared to the background state. This interpretation is supported by the fact that the coagulation rate is proportional to dust surface density, $\Sigma_{d,0} + \delta\Sigma_d$. Lower surface density delays coagulation and results in smaller dust sizes than the background sizes $\tau_{s,0}$, although dust still grows in size (see Figure 1).

Solving the eigenvalue problem with Equations (10)–(12), we obtain the following dispersion relation:

$$n = n_{\text{ap},\pm} \equiv -ikv_{x,0} + \frac{\varepsilon}{6t_0} \left(1 \pm \sqrt{1 - \frac{12t_0}{\varepsilon} \frac{1 - \tau_{s,0}^2}{1 + \tau_{s,0}^2} ikv_{x,0}} \right). \quad (13)$$

There is one growing mode, $n = n_{\text{ap},+}$. For short-wavelength perturbations, the complex growth rate of the growing mode

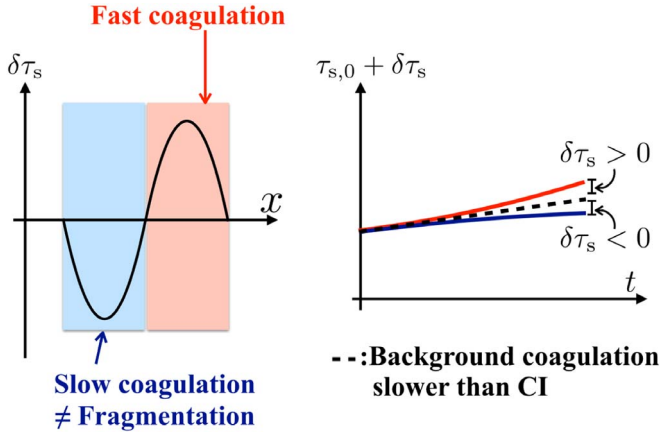


Figure 1. Schematic picture to show the interpretation of wave-like perturbations on τ_s and time evolution of $\tau_{s,0} + \delta\tau_s$ along with the background coagulation and coagulation instability (CI). The sign of $\delta\tau_s$ indicates whether dust sizes are larger or smaller than those expected from the background coagulation. In other words, positive $\delta\tau_s$ means fast coagulation while negative $\delta\tau_s$ means slow coagulation. We note that the negative $\delta\tau_s$ does not mean fragmentation, because we only consider coagulation in Equation (9). We also note that our linear analyses focus on shorter-term evolution via CI than $3t_0/\varepsilon$, such that the background evolution is insignificant although the right figure depicts the background evolution.

can be approximated as

$$\begin{aligned} n_{\text{ap},+} &\simeq -ikv_{x,0} + \frac{\varepsilon}{6t_0} \left(1 + \sqrt{\frac{12t_0}{\varepsilon} \frac{1 - \tau_{s,0}^2}{1 + \tau_{s,0}^2}} ik|v_{x,0}| \right) \\ &= -ikv_{x,0} + \frac{\varepsilon}{6t_0} \left(1 + (1+i) \sqrt{\frac{6t_0}{\varepsilon} \frac{1 - \tau_{s,0}^2}{1 + \tau_{s,0}^2}} k|v_{x,0}| \right). \end{aligned} \quad (14)$$

Thus, the growth rate, i.e., the real part of n , at large $k > 0$ is

$$\begin{aligned} \text{Re}[n_{\text{ap},+}] &\simeq \frac{\varepsilon}{6t_0} \left(1 + \sqrt{\frac{6t_0}{\varepsilon} \frac{1 - \tau_{s,0}^2}{1 + \tau_{s,0}^2}} k|v_{x,0}| \right) \\ &\simeq \frac{\varepsilon}{3t_0} \sqrt{\frac{3t_0}{2\varepsilon} \frac{1 - \tau_{s,0}^2}{1 + \tau_{s,0}^2}} k|v_{x,0}|. \end{aligned} \quad (15)$$

Equation (15) shows that a disk is unconditionally unstable. The growth rate is much larger than $\varepsilon/3t_0$ at wavenumbers that satisfy $t_0 k|v_{x,0}|/\varepsilon \gg 1$. Therefore, this instability develops faster than the unperturbed state that evolves at the timescale of $3t_0/\varepsilon$. The left panel of Figure 2 shows the growth rate as a function of kH for $(\tau_{s,0}, \varepsilon) = (10^{-2}, 10^{-2})$, $(10^{-1}, 10^{-2})$, and $(10^{-1}, 10^{-3})$. The vertical axis is normalized by the coagulation timescale and thus shows how fast coagulation instability grows compared to background coagulation. Equation (15) and Figure 2 show that coagulation instability proceeds faster than background coagulation, in particular for low dust-to-gas ratios.

The relative amplitude of $\delta\tau_s$ to $\delta\Sigma_d$ is

$$\frac{\delta\tau_s/\tau_{s,0}}{\delta\Sigma_d/\Sigma_{d,0}} = \frac{n + ikv_{x,0}}{ik|v_{x,0}|} \frac{1 + \tau_{s,0}^2}{1 - \tau_{s,0}^2}. \quad (16)$$

At short wavelengths, the relative amplitude is approximately given as

$$\begin{aligned} \frac{\delta\tau_s/\tau_{s,0}}{\delta\Sigma_d/\Sigma_{d,0}} &\simeq (1-i) \frac{\varepsilon}{6t_0} \sqrt{\frac{6t_0}{\varepsilon k|v_{x,0}|} \frac{1 + \tau_{s,0}^2}{1 - \tau_{s,0}^2}}, \\ &= \exp\left(-i\frac{\pi}{4}\right) \sqrt{\frac{\varepsilon}{3t_0 k|v_{x,0}|} \frac{1 + \tau_{s,0}^2}{1 - \tau_{s,0}^2}}. \end{aligned} \quad (17)$$

The growth rate is m . This shows that $\delta\tau_s/\tau_{s,0}$ is smaller than $\delta\Sigma_d/\Sigma_{d,0}$ at short wavelengths ($k^{-1} < 3t_0|v_{x,0}|/\varepsilon$), and its phase is shifted outward by $\pi/4$.

Characteristic length of the coagulation instability is $L_{\text{gdl}} \equiv 3t_0|v_{x,0}|/\varepsilon$, which we call a ‘‘growth-drift length.’’ The growth-drift length represents a distance that dust grains move with the unperturbed velocity during the e -folding timescale of dust-size growth. The ratios L_{gdl}/H and L_{gdl}/R are given by

$$\frac{L_{\text{gdl}}}{H} = 3 \left(\frac{t_0\Omega}{0.5} \right) \left(\frac{\varepsilon}{0.01} \right)^{-1} \left(\frac{|v_{x,0}|/c_s}{0.02} \right), \quad (18)$$

$$\begin{aligned} \frac{L_{\text{gdl}}}{R} &= 0.15 \left(\frac{t_0\Omega}{0.5} \right) \left(\frac{\varepsilon}{0.01} \right)^{-1} \left(\frac{|v_{x,0}|/R\Omega}{10^{-3}} \right), \\ &\simeq 0.15 \left(\frac{t_0\Omega}{0.5} \right) \left(\frac{\varepsilon}{0.01} \right)^{-1} \left(\frac{\tau_{s,0}}{0.1} \right) \left(\frac{\eta}{5 \times 10^{-3}} \right). \end{aligned} \quad (19)$$

The growth rate is m . In the last equality, we approximate $|v_{x,0}|$ as $2\tau_{s,0}\eta R\Omega$. One can obtain a universal form of the dispersion relation by scaling wavelengths by the growth-drift length. The right panel of Figure 2 shows the growth rate as a function of kL_{gdl} , showing the universal relation between $\text{Re}[n](\varepsilon/3t_0)^{-1}$ and kL_{gdl} . Using L_{gdl} to normalize a wavenumber $\tilde{k} \equiv kL_{\text{gdl}}$ and assuming $\tilde{k} \gg 1$, we obtain

$$n_{\text{ap},+} \simeq i \frac{\varepsilon}{3t_0} \tilde{k} + \frac{\varepsilon}{6t_0} \left(1 + (1+i) \sqrt{\frac{1 - \tau_{s,0}^2}{1 + \tau_{s,0}^2}} 2\tilde{k} \right). \quad (20)$$

The growth rate normalized by $\varepsilon/3t_0$ is then given by

$$\text{Re}[n_{\text{ap},+}] \left(\frac{3t_0}{\varepsilon} \right) = \frac{1}{2} + \frac{1}{2} \sqrt{\frac{1 - \tau_{s,0}^2}{1 + \tau_{s,0}^2}} 2\tilde{k}. \quad (21)$$

When dust particles are small and $\tau_{s,0} \lesssim 0.1$, we can approximate $1 \pm \tau_{s,0}^2 \simeq 1$ with errors of only a few percent. This approximation gives the growth rate apparently independent of $\tau_{s,0}$:

$$\text{Re}[n_{\text{ap},+}] \left(\frac{3t_0}{\varepsilon} \right) = \frac{1}{2} + \sqrt{\frac{\tilde{k}}{2}}. \quad (22)$$

We note that k is normalized by L_{gdl} , which depends on $|v_{x,0}|$, and hence on $\tau_{s,0}$. Equation (22) shows that the coagulation instability of different size particles can grow at the same rate relative to background coagulation but at different wavelengths $\lambda \propto L_{\text{gdl}}$.

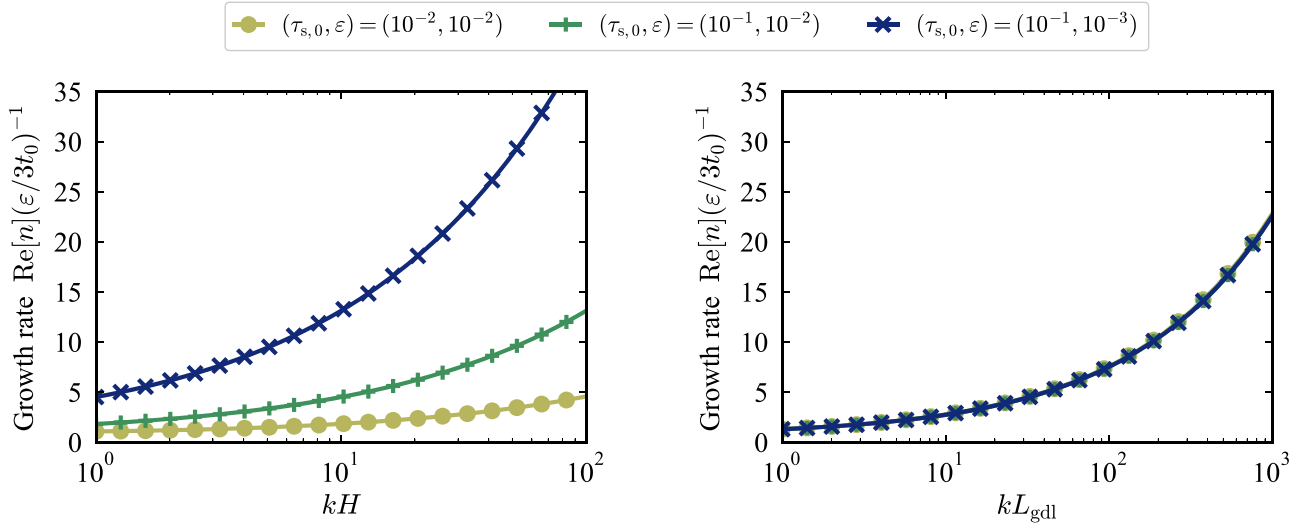


Figure 2. Growth rate of coagulation instability obtained from the simplified linear analyses. The left panel shows the growth rate normalized by $\varepsilon/3t_0$ as a function of kH . As expected from Equation (15), the coagulation instability grows faster than background coagulation, which is more remarkable for $\varepsilon = 10^{-3}$. The right panel shows the growth rates as a function of kL_{gdl} . The growth rate is almost self-similar, as shown by Equations (21) and (22). In both panels, yellow, green, and blue lines show growth rates for $(\tau_{s,0}, \varepsilon) = (10^{-2}, 10^{-2})$, $(10^{-1}, 10^{-2})$, and $(10^{-1}, 10^{-3})$, respectively.

Mechanism of Coagulation Instability

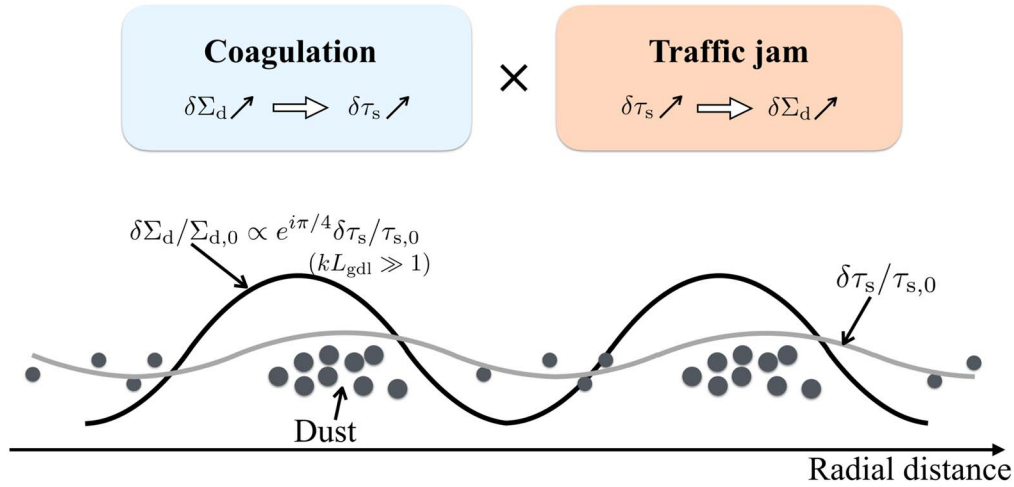


Figure 3. Schematic picture of eigenfunctions of coagulation instability for $kL_{\text{gdl}} \gg 1$. Black and gray lines depict sinusoidal perturbations of $\delta\Sigma_d$ and $\delta\tau_s$, respectively. The sizes of filled circles represent dust sizes. Coagulation instability is driven by a combination of coagulation and traffic jam. Because coagulation efficiency is proportional to dust surface density $\Sigma_{d,0} + \delta\Sigma_d$ (Equation (9)), dust surface density perturbations lead to radial variation of dust sizes and $\delta\tau_s$. The radial variation of $\delta\tau_s$ leads to traffic jam and amplifies $\delta\Sigma_d$. This positive feedback process triggers coagulation instability.

2.2.2. Physical Mechanism of Coagulation Instability

Coagulation instability is triggered by a combination of coagulation and traffic jam. In fact, the growth rate at short wavelengths is determined by the geometric mean of coagulation rate, $\varepsilon/3t_0$, and a rate of traffic jam, $[(1 - \tau_{s,0}^2)/(1 + \tau_{s,0}^2)]k|v_{x,0}|$ (see Equation (15)). Figure 3 shows a schematic picture of eigenfunctions of $\delta\Sigma_d$ and $\delta\tau_s$. When there is a perturbation in dust surface density, dust particles grow more efficiently in regions of $\delta\Sigma_d > 0$. On the other hand, dust particles grow less efficiently at regions of $\delta\Sigma_d < 0$. Such a spatial variation of the coagulation efficiency leads to perturbations in dust sizes and thus $\delta\tau_s$. Perturbations in $\delta\tau_s$ lead to traffic jam in the radial direction and further amplify $\delta\Sigma_d$. In this way, coagulation and traffic jam act as a positive feedback process and make a disk unstable.

As noted above, the unstable mode at short wavelengths has a phase shift of $\pi/4$ between $\delta\Sigma_d$ and $\delta\tau_s$. Phase shift is sometimes important in the growth mechanism of dust–gas instabilities (e.g., streaming instability; see Lin & Youdin 2017). The origin of the phase shift in coagulation instability can be explained based on the obtained dispersion relation and a toy-model equation described below. For simplicity, we focus on short-wavelength perturbations so that we can use Equation (14) and further simplify as follows:

$$n_{\text{ap},+} \simeq -ikv_{x,0} + \frac{\varepsilon(1+i)}{6t_0} \sqrt{\frac{6t_0(1-\tau_{s,0}^2)}{\varepsilon(1+\tau_{s,0}^2)}k|v_{x,0}|}. \quad (23)$$

One can see that waves of the phase velocity $v_{\text{ph}} = -\text{Im}[n_{\text{ap},+}]/k$ move inward faster than dust grains drifting at $v_{x,0}$. The relative

velocity $\Delta v_{d,w}$ is

$$\Delta v_{d,w} \equiv v_{x,0} - v_{\text{ph}} = \frac{\varepsilon}{6t_0} \sqrt{\frac{6t_0}{\varepsilon} \frac{1 - \tau_{s,0}^2}{1 + \tau_{s,0}^2} \frac{|v_{x,0}|}{k}}. \quad (24)$$

In other words, dust grains move outward at the wave-rest frame. One key property is $\text{Re}[n_{\text{ap},+}] = \Delta v_{d,w} k$, meaning that the e -folding time of $\delta\tau_s$ and $\delta\Sigma_d$ is equal to a dust-crossing time over the length of k^{-1} at the short-wavelength limit. To discuss coagulation efficiency in the presence of waves of $\delta\Sigma_d$, we consider the following toy-model equation of $\delta\tau_s$ evolution at the wave-rest frame (t, X):

$$\begin{aligned} \frac{d(\delta\tau_s/\tau_{s,0})}{dt} &= \frac{\varepsilon}{3t_0} \frac{\delta\Sigma_d}{\Sigma_{d,0}} \\ &= \frac{\varepsilon}{3t_0} \frac{|\delta\Sigma_d(t=0)|}{\Sigma_{d,0}} \\ &\quad \times \exp(\text{Re}[n_{\text{ap},+}]t) \cos(k(X_0 + \Delta X)) \\ &= \frac{\varepsilon}{3t_0} \frac{|\delta\Sigma_d(t=0)|}{\Sigma_{d,0}} \\ &\quad \times \exp(k\Delta v_{d,w}t) \cos(kX_0 + k\Delta v_{d,w}t), \end{aligned} \quad (25)$$

where X_0 and ΔX are the initial position of dust grains and a distance over which dust grains move. In the last equality, we utilize $\Delta X = \Delta v_{d,w}t$ and $\text{Re}[n_{\text{ap},+}] = \Delta v_{d,w}k$, which are noted above. We note that we neglect the growth of background state $\tau_{s,0}$ because $\text{Re}[n_{\text{ap},+}]$ is larger than the coagulation rate at the short wavelengths considered. The solution of Equation (25) is

$$\frac{\delta\tau_s(t) - \delta\tau_s(t=0)}{\tau_{s,0}} = \frac{\varepsilon}{3\sqrt{2}t_0k\Delta v_{d,w}} \frac{|\delta\Sigma_d|}{\Sigma_{d,0}} F(k\Delta v_{d,w}t, kX_0), \quad (26)$$

$$\begin{aligned} F(k\Delta v_{d,w}t, kX_0) &\equiv \exp(k\Delta v_{d,w}t) \\ &\quad \times \cos\left(k\Delta v_{d,w}t + kX_0 - \frac{\pi}{4}\right) \\ &\quad - \cos\left(kX_0 - \frac{\pi}{4}\right). \end{aligned} \quad (27)$$

One can ask what is the value of X_0 that maximizes the size of dust grains moving across one wavelength, i.e., $k\Delta v_{d,w}t = 2\pi$.³ Considering $0 \leq kX_0 < 2\pi$ without loss of generality, we find that $F(2\pi, kX_0)$ is the largest for $kX_0 = \pi/4$ (see Equation (27)). Therefore, dust grains that start moving from $X_0 = \pi/4k$ grow the most efficiently, which explains the peak position of $\delta\tau_s$ that is shifted by $\pi/4$ in phase relative to $\delta\Sigma_d$.

We note that substituting $k=0$ in Equation (13) gives $n_{\text{ap},+} = \varepsilon/3t_0$, i.e., the coagulation rate. The associated eigenfunction is $\delta\Sigma_d = 0$, $\delta\tau_s \neq 0$, and thus $\delta v_x \neq 0$. This mode is just coagulation and not the pileup via instabilities. Because of its infinitely long wavelength ($k=0$), one can regard this mode as a shift in stopping time, i.e., dust sizes, from $\tau_{s,0}$ to $\tau_{s,0} + \delta\tau_s$. The size-shifted dust grains coagulate at a rate of $\varepsilon/3t_0$, which is the physical explanation of the $k=0$ mode. Note, however, that our linear analyses are valid for $n > \varepsilon/3t_0$ (or $kL_{\text{gdl}} \gg 1$) as mentioned above.

³ The periodicity of sinusoidal perturbations justifies the choice of $k\Delta v_{d,w}t = 2\pi$.

3. Two-fluid Linear Analyses

In this section, we perform two-fluid linear analyses and discuss effects of the gas density profile and nonsteady gas motion on the coagulation instability. As noted in the previous section, the coagulation rate is determined not by dust-to-gas ratio in a dust layer, but by the total dust-to-gas surface density ratio Σ_d/Σ_g . This motivates us to first use two-fluid equations averaged over the full vertical extent of a disk. When the gas layer turbulence is weak and the vertical momentum exchange/transfer is very limited in a gas disk, the dust-gas momentum exchange should be averaged within a ‘‘sublayer’’ around the midplane rather than for a whole disk. We will also analyze such limiting cases of weak turbulence in Appendix C. We find, however, that such a sublayer model shows insignificant differences when a sublayer height z_s is larger than $3H_d$. Thus, we describe full-disk averaging model in this section (see Section 4.2 for discussions regarding the combined effects of size-dependent settling and reduced drift velocity).

The hydrodynamic equations are

$$\frac{\partial\Sigma_g}{\partial t} + \frac{\partial\Sigma_g u_x}{\partial x} = 0, \quad (28)$$

$$\frac{\partial u_x}{\partial t} + u_x \frac{\partial u_x}{\partial x} = 3\Omega^2 x + 2\Omega u_y - \frac{1}{\Sigma_g} \frac{\partial c_s^2 \Sigma_g}{\partial x} + \frac{\Sigma_d}{\Sigma_g} \frac{v_x - u_x}{\tau_s} \Omega, \quad (29)$$

$$\frac{\partial u_y}{\partial t} + u_x \frac{\partial u_y}{\partial x} = -2\Omega u_x + \frac{\Sigma_d}{\Sigma_g} \frac{v_y - u_y}{\tau_s} \Omega, \quad (30)$$

$$\frac{\partial\Sigma_d}{\partial t} + \frac{\partial\Sigma_d v_x}{\partial x} = 0, \quad (31)$$

$$\frac{\partial v_x}{\partial t} + v_x \frac{\partial v_x}{\partial x} = 3\Omega^2 x + 2\Omega v_y - \frac{v_x - u_x}{\tau_s} \Omega, \quad (32)$$

$$\frac{\partial v_y}{\partial t} + v_x \frac{\partial v_y}{\partial x} = -2\Omega v_x - \frac{v_y - u_y}{\tau_s} \Omega, \quad (33)$$

where u_x and u_y are the radial and azimuthal gas velocities, and v_y is the azimuthal dust velocity.

Equations (4), (7), and (28) give the evolutionary equation of τ_s :

$$\frac{\partial\tau_s}{\partial t} + v_x \frac{\partial\tau_s}{\partial x} = \frac{\Sigma_d}{\Sigma_g} \frac{\tau_s}{3t_0} + \frac{\tau_s}{\Sigma_g} \frac{\partial\Sigma_g u_x}{\partial x} - \frac{\tau_s}{\Sigma_g} v_x \frac{\partial\Sigma_g}{\partial x}, \quad (34)$$

The second term on the right-hand side is the effect of the gas compression that decreases τ_s . The third term represents a process where τ_s decreases as dust particles drift with v_x toward the inner high-gas-density region. Note that these terms with the gas surface density gradients originate from Σ_g in the drag law adopted for the midplane dust (Equation (7)). Equation (7) is valid as long as the gas density has the vertical Gaussian profile. Therefore, whatever vertical extent is adopted in the vertical averaging of the equations, the total gas surface density appears in Equation (34).

3.1. Unperturbed State

As in the simplified one-fluid analyses, we construct the unperturbed state without using Equation (34) (see also Appendix B). Neglecting Equation (34) in the unperturbed state is valid because coagulation instability grows faster than the background coagulation proceeds. The steady state is then

governed by the following equations:

$$\frac{\partial \Sigma_g u_x}{\partial x} = 0, \quad (35)$$

$$u_x \frac{\partial u_x}{\partial x} = 3\Omega^2 x + 2\Omega u_y - \frac{1}{\Sigma_g} \frac{\partial c_s^2 \Sigma_g}{\partial x} + \frac{\Sigma_d}{\Sigma_g} \frac{v_x - u_x}{\tau_s} \Omega, \quad (36)$$

$$u_x \frac{\partial u_y}{\partial x} = -2\Omega u_x + \frac{\Sigma_d}{\Sigma_g} \frac{v_y - u_y}{\tau_s} \Omega, \quad (37)$$

$$\frac{\partial \Sigma_d v_x}{\partial x} = 0, \quad (38)$$

$$v_x \frac{\partial v_x}{\partial x} = 3\Omega^2 x + 2\Omega v_y - \frac{v_x - u_x}{\tau_s} \Omega, \quad (39)$$

$$v_x \frac{\partial v_y}{\partial x} = -2\Omega v_x - \frac{v_y - u_y}{\tau_s} \Omega. \quad (40)$$

Coagulation instability requires the dust drift motion, which occurs in the presence of a global gas pressure gradient, i.e., the drift velocities are proportional to the gradient. We thus seek a dust drift solution considering a globally smooth gas disk with small radial gradients of surface density $\Sigma'_{g,0} \equiv \partial \Sigma_{g,0} / \partial x$ and gas pressure $(c_s^2 \Sigma_{g,0})' \equiv \partial (c_s^2 \Sigma_{g,0}) / \partial x$. We do not consider a characteristic structure (e.g., a bump) in a disk, and assume the spatial scale of surface density and pressure variations to be of the order of radius R : $\Sigma'_{g,0} / \Sigma_{g,0} \sim R^{-1}$ and $(c_s^2 \Sigma_{g,0})' / c_s^2 \Sigma_{g,0} \sim R^{-1}$. Linear analyses with a bump structure can be found in Auffinger & Laibe (2018), where they perform linear analyses of streaming instability with dust drifting in an enforced pressure bump. In this work, we approximately derive a drift solution with the following assumptions. First, we assume the small radial size of the local frame, ΔR , and $|x|/R < \Delta R/R \ll 1$. Besides the smallness of the local frame, we also assume that $(c_s^2 \Sigma_{g,0})'$, $\Sigma'_{g,0}$, and gradients of the other unperturbed quantities are so small that we can neglect the second- and higher-order terms of the gradients. Based on these assumptions, we find the following solution that satisfies Equations (35)–(40) to the first order in x/R :

$$u_x = u_{x,0} \equiv \frac{2\varepsilon \tau_{s,0}}{(1 + \varepsilon)^2 + \tau_{s,0}^2} \left(-\frac{(c_s^2 \Sigma_{g,0})'}{2\Omega \Sigma_{g,0}} \right), \quad (41)$$

$$u_y = -\frac{3}{2} \Omega x + u_{y,0}, \quad (42)$$

$$u_{y,0} \equiv -\left[1 + \frac{\varepsilon \tau_{s,0}^2}{(1 + \varepsilon)^2 + \tau_{s,0}^2} \right] \left(-\frac{(c_s^2 \Sigma_{g,0})'}{2\Omega \Sigma_{g,0} (1 + \varepsilon)} \right), \quad (43)$$

$$v_x = v_{x,0} \equiv -\frac{2\tau_{s,0}}{(1 + \varepsilon)^2 + \tau_{s,0}^2} \left(-\frac{(c_s^2 \Sigma_{g,0})'}{2\Omega \Sigma_{g,0}} \right), \quad (44)$$

$$v_y = -\frac{3}{2} \Omega x + v_{y,0}, \quad (45)$$

$$v_{y,0} \equiv -\left[1 - \frac{\tau_{s,0}^2}{(1 + \varepsilon)^2 + \tau_{s,0}^2} \right] \left(-\frac{(c_s^2 \Sigma_{g,0})'}{2\Omega \Sigma_{g,0} (1 + \varepsilon)} \right), \quad (46)$$

where the subscript ‘‘0’’ denotes unperturbed quantities, and $\varepsilon = \Sigma_{d,0} / \Sigma_{g,0}$, $(c_s^2 \Sigma_{g,0})'$ and $\tau_{s,0}$ are input parameters in this formalism. Note that the drift velocities are of the first order in the small gradient (i.e., $(c_s^2 \Sigma_{g,0})'$), and thus in x/R , because of

the nature of the dust drift. We describe the details of the derivation in Appendix B.

The drift solution in the two-fluid height-integrated systems is characterized by

$$\eta_{2D} \equiv -\frac{(c_s^2 \Sigma_{g,0})'}{2R\Omega^2 \Sigma_{g,0}}. \quad (47)$$

The drift velocity with η_{2D} is the reasonable solution in the two-fluid height-integrated system with the full-disk averaging. However, η_{2D} is different from η because only the latter includes the radial profile of H , which prevents direct comparison with the growth rates and the phase velocities obtained in the previous section because the drift velocities are different. We thus compromise by using the value of η with an assumed disk model and substituting it into η_{2D} of Equation (47) to calculate $(c_s^2 \Sigma_{g,0})'$ and the drift velocities, i.e.,

$$-\frac{(c_s^2 \Sigma_{g,0})'}{\Sigma_{g,0}} = 2\eta_{2D} R\Omega^2 \rightarrow 2\eta R\Omega^2. \quad (48)$$

Assuming the temperature profile, we obtain $\Sigma'_{g,0}$ from the following equation:

$$\frac{\Sigma'_{g,0}}{\Sigma_{g,0}} = -\frac{1}{R} \left(2\eta_{2D} \frac{R^2 \Omega^2}{c_s^2} + \frac{\partial \ln c_s^2}{\partial \ln R} \right). \quad (49)$$

The definition of η (Equation (3)) gives

$$\frac{\Sigma'_{g,0}}{\Sigma_{g,0}} = -\frac{1}{R} \left(2\eta \frac{R^2 \Omega^2}{c_s^2} + \frac{\partial \ln c_s^2}{\partial \ln R} - \frac{\partial \ln H}{\partial \ln R} \right). \quad (50)$$

Thus, substituting the value of η in η_{2D} in Equation (49) gives smaller $\Sigma'_{g,0} / \Sigma_{g,0}$.⁴

In the following subsection, we calculate $\Sigma'_{g,0}$ by using Equation (49) with an assumed value of η . We again note that the above calculation of $\Sigma'_{g,0}$ and η_{2D} with an assumed value of η is only for enabling the direct comparison of results obtained in one-fluid and two-fluid analyses (see Section 4.2).

3.2. Linearized Equations

Based on the above unperturbed state, we derive the linearized equations assuming perturbations $\delta \Sigma_g$, δu_x , δu_y , $\delta \Sigma_d$, δv_x , δv_y , and $\delta \tau_s$ proportional to $\exp(ikx + nt)$. Because of the gas density and pressure profile with $\Sigma'_{g,0} x / \Sigma_{g,0} \sim (c_s^2 \Sigma_{g,0})' x / (c_s^2 \Sigma_{g,0}) \sim x/R \ll 1$ (see Appendix B), the amplitudes of these perturbations depend on x in general. In this study, focusing on short-wavelength perturbations with $kR \gg 1$ ($|x| < \Delta R$, $\Delta R/R \ll 1$), we assume that the spatial variation of $\exp(ikx)$ is larger than that of the perturbation amplitudes, such that we can approximate $\partial \delta A / \partial x \simeq ik \delta A$, where δA represents a perturbed physical quantity (e.g., $\delta \Sigma_d$). This approximation corresponds to the WKB approximation (e.g., see Shu 1992). We also assume that the temperature profile remains steady. The linearized equations are

$$(n + ik u_{x,0}) \delta \Sigma_g + \left(ik \Sigma_{g,\text{unp}} + \frac{\partial \Sigma_{g,\text{unp}}}{\partial x} \right) \delta u_x = 0, \quad (51)$$

⁴ Note that we only consider the case that $\Sigma'_{g,0} / \Sigma_{g,0}$ is negative.

$$\begin{aligned}
(n + ikv_{x,0})\delta u_x &= 2\Omega\delta u_y + \frac{c_s^2\delta\Sigma_g}{\Sigma_{g,\text{unp}}^2} \frac{\partial\Sigma_{g,\text{unp}}}{\partial x} \\
&\quad - \frac{c_s^2}{\Sigma_{g,\text{unp}}} ik\delta\Sigma_g \\
&\quad + \frac{\Sigma_{d,0}}{\Sigma_{g,\text{unp}}} \frac{v_{x,0} - u_{x,0}}{\tau_{s,0}} \Omega \\
&\quad \times \left(\frac{\delta\Sigma_d}{\Sigma_{d,0}} - \frac{\delta\Sigma_g}{\Sigma_{g,\text{unp}}} + \frac{\delta v_x - \delta u_x}{v_{x,0} - u_{x,0}} - \frac{\delta\tau_s}{\tau_{s,0}} \right), \tag{52}
\end{aligned}$$

$$\begin{aligned}
(n + ikv_{x,0})\delta u_y &= -\frac{\Omega}{2}\delta u_x \\
&\quad + \frac{\Sigma_{d,0}}{\Sigma_{g,\text{unp}}} \frac{v_{y,0} - u_{y,0}}{\tau_{s,0}} \Omega \\
&\quad \times \left(\frac{\delta\Sigma_d}{\Sigma_{d,0}} - \frac{\delta\Sigma_g}{\Sigma_{g,\text{unp}}} + \frac{\delta v_y - \delta u_y}{v_{y,0} - u_{y,0}} - \frac{\delta\tau_s}{\tau_{s,0}} \right), \tag{53}
\end{aligned}$$

$$(n + ikv_{x,0})\delta\Sigma_d + ik\Sigma_{d,0}\delta v_x = 0, \tag{54}$$

$$\begin{aligned}
(n + ikv_{x,0})\delta v_x &= 2\Omega\delta v_y \\
&\quad - \frac{v_{x,0} - u_{x,0}}{\tau_{s,0}} \Omega \left(\frac{\delta v_x - \delta u_x}{v_{x,0} - u_{x,0}} - \frac{\delta\tau_s}{\tau_{s,0}} \right), \tag{55}
\end{aligned}$$

$$\begin{aligned}
(n + ikv_{x,0})\delta v_y &= -\frac{\Omega}{2}\delta v_x \\
&\quad - \frac{v_{y,0} - u_{y,0}}{\tau_{s,0}} \Omega \left(\frac{\delta v_y - \delta u_y}{v_{y,0} - u_{y,0}} - \frac{\delta\tau_s}{\tau_{s,0}} \right), \tag{56}
\end{aligned}$$

$$\begin{aligned}
(n + ikv_{x,0})\delta\tau_s &= \frac{\Sigma_{d,0}}{\Sigma_{g,\text{unp}}} \frac{\tau_{s,0}}{3t_0} \left(\frac{\delta\Sigma_d}{\Sigma_{d,0}} - \frac{\delta\Sigma_g}{\Sigma_{g,\text{unp}}} + \frac{\delta\tau_s}{\tau_{s,0}} \right) \\
&\quad + \frac{\tau_{s,0}}{\Sigma_{g,\text{unp}}} \left[\left(ik\Sigma_{g,\text{unp}} + \frac{\partial\Sigma_{g,\text{unp}}}{\partial x} \right) \delta u_x \right. \\
&\quad \left. + ikv_{x,0}\delta\Sigma_g \right] - \frac{\tau_{s,0}v_{x,0}}{\Sigma_{g,\text{unp}}} ik\delta\Sigma_g \\
&\quad - \frac{\tau_{s,0}v_{x,0}}{\Sigma_{g,\text{unp}}} \frac{\partial\Sigma_{g,\text{unp}}}{\partial x} \left(\frac{\delta\tau_s}{\tau_{s,0}} + \frac{\delta v_x}{v_{x,0}} - \frac{\delta\Sigma_g}{\Sigma_{g,\text{unp}}} \right), \tag{57}
\end{aligned}$$

where $\Sigma_{g,\text{unp}} \equiv \Sigma_{g,0} + \Sigma'_{g,0}x$. The complex growth rate n is derived from the above equations with $x = 0$, i.e., $\Sigma_{g,\text{unp}} = \Sigma_{g,0}$.

We note that one finds $|\partial\Sigma_{g,\text{unp}}/\partial x| \ll k\Sigma_{g,\text{unp}}$ based on the assumption of the unperturbed gas profiles with the small gradients (e.g., $\Sigma'_{g,0}x/\Sigma_{g,0} \sim x/R \ll 1$) and short-wavelength perturbations ($kR \gg 1$). Neglecting the gradients of the unperturbed profiles in the linearized equations, one finds that the resulting equations of motion and continuity equations are equivalent to linearized equations that can be derived with a uniform background state and an external force on gas to drive the drift motion except for $\delta\tau_s$ (e.g., see Tominaga et al. 2020)⁵

⁵ Equations used in Tominaga et al. (2020) include self-gravity, viscosity, dust diffusion, and dust velocity dispersion, which are not considered in this section. Except for that difference and $\delta\tau_s$ in the present equations, one finds the equivalent equations for $|\partial\Sigma_{g,\text{unp}}/\partial x| \ll k\Sigma_{g,\text{unp}}$.

Therefore, the present analyses give almost the same growth rate at $kR \gg 1$ as one derived from linear analyses with the often-used external force. In other words, our analyses justify the use of the external force driving the drift to study mode properties at short wavelengths.

3.3. Growth Rate and Phase Velocity

The parameters in this analysis are ε , $\tau_{s,0}$, η_{2D} , and the power-law index of c_s^2 (see Equation (49)). As noted above, we substitute the value of η into η_{2D} to compare the one-fluid and two-fluid analyses. We refer to the MMSN model (Hayashi 1981) with a solar-mass star to assume the value of η and $\partial \ln c_s^2 / \partial R$. In the MMSN model, the gas surface density and the temperature T are given by $\Sigma_{g,\text{MMSN}} = 1700(R/1 \text{ au})^{-3/2} \text{ g cm}^{-2}$ and $T = 280(R/1 \text{ au})^{-1/2} \text{ K}$. Based on the disk model with the midplane gas density $\rho_{g,\text{MMSN}}(0) = \Sigma_{g,\text{MMSN}}/\sqrt{2\pi}H$ and the mean molecular weight of 2.34, one obtains $\eta \simeq 1.81 \times 10^{-3}(R/1 \text{ au})^{1/2}$ and $\partial \ln c_s^2 / \partial \ln R = -0.5$.

Substituting the above value of η at a given R in η_{2D} in Equation (49), we calculate the growth rate and the phase velocity. As noted in Section 3.1, the $\Sigma'_{g,0}/\Sigma_{g,0}$ used in this section is smaller than $\Sigma_{g,\text{MMSN}}'/\Sigma_{g,\text{MMSN}}$ because of the replacement of η_{2D} by η . At $R = 20 \text{ au}$, we obtain $\Sigma'_{g,0}/\Sigma_{g,0} \simeq -0.19H^{-1}$ and $\Sigma_{g,\text{MMSN}}'/\Sigma_{g,\text{MMSN}} \simeq -0.11H^{-1}$.

Figure 4 shows the growth rate $\text{Re}[n]$ normalized by $\varepsilon/3t_0$ and the phase velocity $v_{\text{ph}} \equiv -\text{Im}[n]/k$ normalized by $|v_{x,0}|$ in the case of $\tau_{s,0} = 0.1$, $\varepsilon = 10^{-3}$, and $R = 20 \text{ au}$. The value of η in this case is $\eta \simeq 0.00809$. We also plot the growth rate and the phase velocity derived from the one-fluid analyses (Equation (13)). The k -dependences of the growth rates from both analyses are similar, although the two-fluid analyses give lower growth rates. The phase velocities at high wavenumbers show a good agreement between the one-fluid and two-fluid analyses while the difference is visible at low wavenumbers.

The quantitative differences come from the third term on the right-hand side of Equation (34). The term represents the gas surface density variation during the dust drift. To understand this effect, we perform modified one-fluid analyses with Equation (1) and the following equation:

$$\frac{\partial\tau_s}{\partial t} + v_x \frac{\partial\tau_s}{\partial x} = \frac{\Sigma_d}{\Sigma_g} \frac{\tau_s}{3t_0} - \frac{\tau_s}{\Sigma_g} v_x \frac{\partial\Sigma_g}{\partial x}, \tag{58}$$

In the same way in Section 2, one can derive a dispersion relation of the growing mode:

$$\begin{aligned}
n_{\text{ap}}(k, W) &\equiv -ikv_{x,0} \\
&\quad + \frac{\varepsilon}{6t_0} \left(W + \sqrt{W^2 - \frac{12t_0}{\varepsilon} \frac{1 - \tau_{s,0}^2}{1 + \tau_{s,0}^2} ikv_{x,0}} \right), \tag{59}
\end{aligned}$$

$$W \equiv 1 + \frac{2}{1 + \tau_{s,0}^2} \frac{L_{\text{gdl}}}{\Sigma_{g,0}/\Sigma'_{g,0}}. \tag{60}$$

Considering $\tau_{s,0} \ll 1$, one obtains

$$n_{\text{ap}}(k, W) \simeq -ikv_{x,0} + \frac{\varepsilon}{6t_0} \left(W + \sqrt{W^2 - \frac{12t_0}{\varepsilon} ikv_{x,0}} \right) \tag{61}$$

$$W \simeq 1 + 2 \frac{L_{\text{gdl}}}{\Sigma_{g,0}/\Sigma'_{g,0}}. \tag{62}$$

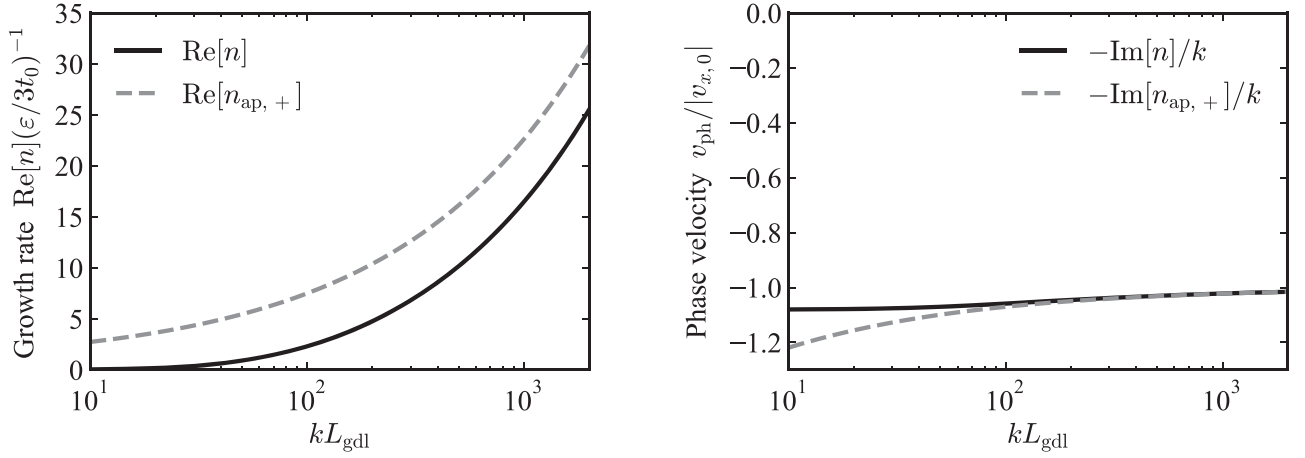


Figure 4. Growth rate and phase velocity obtained from the two-fluid linear analyses for $\tau_{s,0} = 0.1$, $\varepsilon = 10^{-3}$, and $R = 20$ au (black lines). In this case, one has $L_{\text{gdl}} \simeq 33.8H$. The gray dashed lines correspond to the growth rate and the phase velocity of the growing mode in one-fluid analyses (Equation (13)). The k -dependence of growth rate in two-fluid analyses is similar to that in one-fluid analyses, although the two-fluid growth rate is smaller than the one-fluid growth rate. In both analyses, the phase velocities converge to the drift velocity, especially at shorter wavelengths.

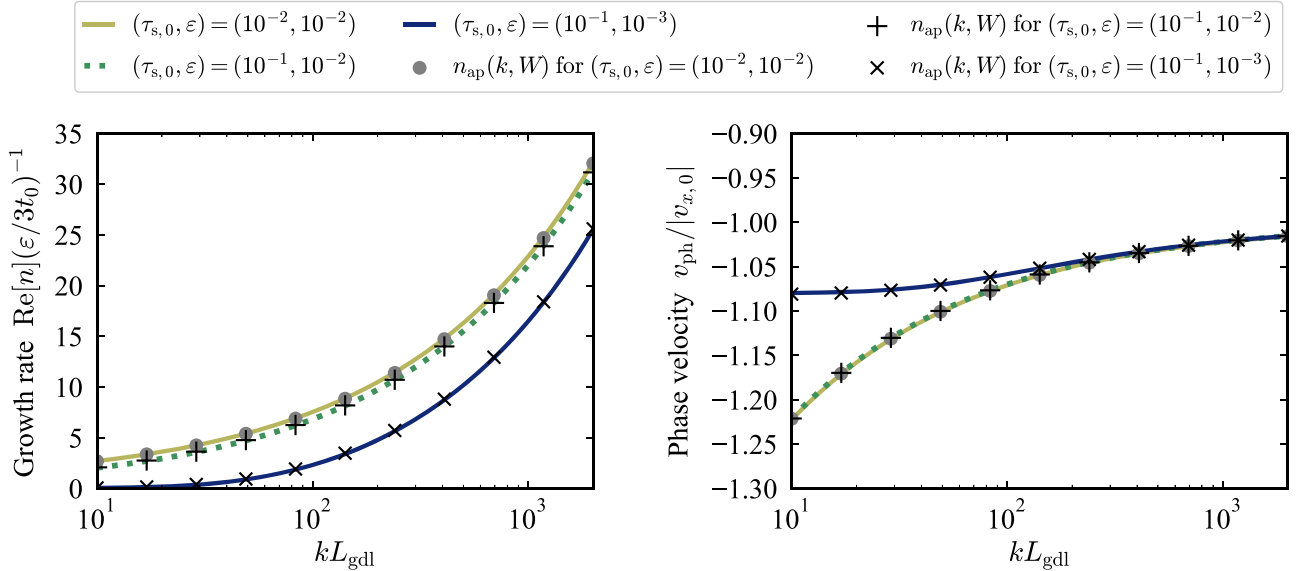


Figure 5. Growth rate and phase velocity for $R = 20$ au. Yellow solid, green dashed, and blue solid lines show the results of the two-fluid analyses for $(\tau_{s,0}, \varepsilon) = (10^{-2}, 10^{-2})$, $(10^{-1}, 10^{-2})$, and $(10^{-1}, 10^{-3})$, respectively. Filled circles, plus marks, and cross marks represent growth rates and phase velocities obtained from the modified one-fluid analyses (Equation (59)). We find that the results of the two-fluid analyses are well-reproduced by the modified one-fluid analyses.

Figure 5 compares the modified one-fluid dispersion relation $n_{\text{ap}}(k, W)$ (Equation (59)) and two-fluid dispersion relation n . The modified one-fluid analyses well-reproduce the results of the two-fluid analyses. Since the gas surface density gradient is negative, the newly introduced factor W is less than unity, which reduces the growth rate. When the growth-drift length is much larger than $|\Sigma_{g,0}/\Sigma'_{g,0}|$, the factor W becomes negative and its absolute value can become larger than unity. In such a case, the growth rate approaches 0 for $k \rightarrow 0$ as shown in Figure 4. The phase velocity is independent of k at small wavenumbers for $W < 0$, and becomes $v_{\text{ph}} \simeq v_{x,0}(1 + 1/|W|)$ for $kL_{\text{gdl}} \ll W^2/4$ and $1 \pm \tau_{s,0}^2 \simeq 1$. This saturation of the phase velocity can be seen as cross marks in Figure 5, where the growth-drift length is about $33.8H$ and $W \simeq -12.0$ from Equation (60), which gives $v_{\text{ph}}/v_{x,0} \simeq 1.08$.

Regardless of the quantitative difference as shown in Figure 4, the simple one-fluid analyses roughly reproduce k -dependence of the growth rate obtained in two-fluid analyses. The modified one-fluid analyses with steady gas surface density gradient better reproduce the two-fluid dispersion relation. Therefore, the coagulation instability is essentially a one-fluid instability (see also Appendix C) and different from the streaming instability and the draft instability (e.g., Youdin & Goodman 2005; Lambrechts et al. 2016).

Figure 6 shows the growth rate as a function of $\tau_{s,0}$ and $\Sigma_{d,0}/\Sigma_{g,0}$. Since the growth rate monotonically increases as kH increases, we fix the wavenumber and take $kH = 60$ as the reference value. The left panel of Figure 6 shows that the growth rate in the unit of Ω increases as the normalized stopping time $\tau_{s,0}$ or the dust-to-gas ratio $\varepsilon = \Sigma_{d,0}/\Sigma_{g,0}$ increases. These trends are consistent with the ε - and

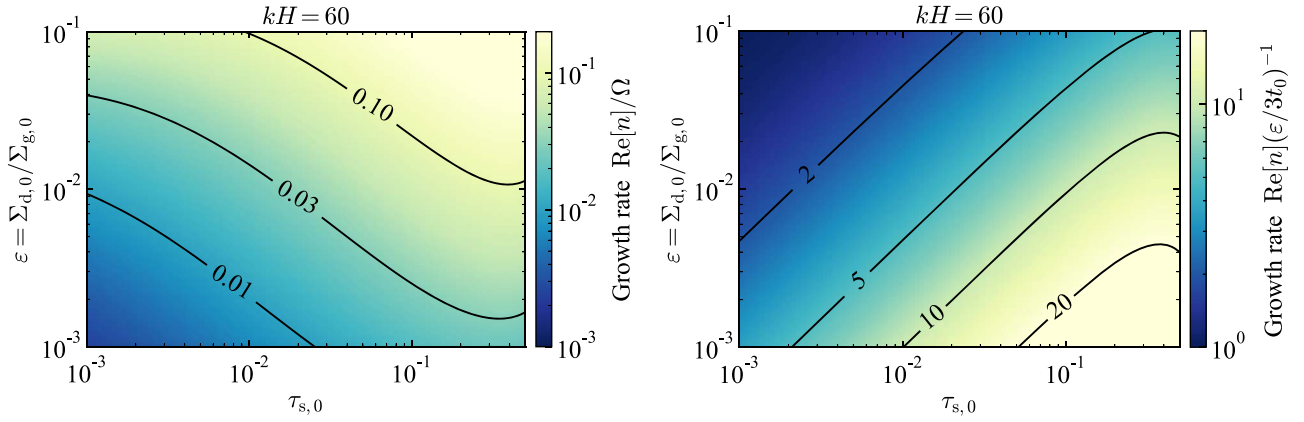


Figure 6. Growth rates obtained from the two-fluid analyses at $kH = 60$ as a function of the normalized stopping time $\tau_{s,0}$ and the unperturbed dust-to-gas surface density ratio $\varepsilon = \Sigma_{d,0}/\Sigma_{g,0}$. Here, we assume $R = 20$ au. The left figure shows the growth rate in the unit of Ω . The growth rates become larger for larger dust sizes, i.e., τ_s is larger because the faster drift speed results in a stronger traffic jam. The growth rates also increase as the dust-to-gas ratio increases, as expected from the one-fluid analyses (see Equation (13)). The right figure shows the growth rate normalized by the coagulation timescale $3t_0/\varepsilon$. The growth rates increase as $\tau_{s,0}/\varepsilon$ increases because $kL_{\text{gdI}} \propto k\tau_{s,0}/\varepsilon$ increases, which is also seen in the one-fluid analyses (see Equation (21)).

$\tau_{s,0}$ -dependences of the dispersion relation from the modified one-fluid analyses. As $\tau_{s,0}$ increases, one obtains larger dust drift speed $|v_{x,0}|$. Because the velocity perturbation is proportional to $v_{x,0}$ (Equation (11)), the faster drift speed results in the stronger concentration, and thus larger growth rates. As ε increases, dust coagulation becomes effective and the coagulation instability grows faster.

The right panel of Figure 6 shows the growth rate normalized by the coagulation timescale $3t_0/\varepsilon$. As shown in Section 2, the dispersion relation obtained from the one-fluid analyses becomes self-similar for $\tau_{s,0} \ll 1$ when one normalizes the growth rate by $3t_0/\varepsilon$ and wavenumbers by the growth-drift length L_{gdI} (Equation (22)). The growth rate $\text{Re}[n]3t_0/\varepsilon$ should be constant for constant $\tau_{s,0}/\varepsilon$ because L_{gdI} is proportional to $|v_{x,0}|/\varepsilon$ and the drift speed is proportional to $\tau_{s,0}$. We find that the right panel of Figure 6 also shows this trend. The modified one-fluid analyses also explain the self-similarity in the two-fluid dispersion relation. From Equation (61), which is valid for $\tau_{s,0} \ll 1$, one obtains

$$n_{\text{ap}}(k, W) \left(\frac{3t_0}{\varepsilon} \right) \simeq i\tilde{k} + \frac{1}{2}(W + \sqrt{W^2 + 4i\tilde{k}}). \quad (63)$$

According to Equation (62), the factor W depends on $\tau_{s,0}$ and ε only through their ratio $\tau_{s,0}/\varepsilon$ in L_{gdI} for $\tau_{s,0} \ll 1$. Therefore, the growth rate is self-similar for a given gas surface density gradient $\Sigma'_{g,0}/\Sigma_{g,0}$.

As already mentioned, we use Equation (49) to calculate $\Sigma'_{g,0}/\Sigma_{g,0}$ with the replacement of η_{2D} by η , leading to $\Sigma'_{g,0}/\Sigma_{g,0} < \Sigma_{g,\text{MMSN}}'/\Sigma_{g,\text{MMSN}} (< 0)$. According to the definition of W , negative $\Sigma'_{g,0}$ and its larger magnitude result in smaller W , which stabilizes the coagulation instability. Thus, the growth rates are underestimated in the current two-fluid analyses to some extent. Because the analyses of this section show that coagulation instability is essentially one-fluid mode (see also Appendix C), we conclude that it will be better to use dispersion relations from modified one-fluid analyses with a “true” gas surface density gradient ($\Sigma_{g,\text{MMSN}}'/\Sigma_{g,\text{MMSN}}$) instead of using two-fluid dispersion relation. We thus adopt a one-fluid approach with a gas surface density gradient in the evolutionary equation for τ_s in the following section.

4. Discussion

4.1. Stabilization Due to Dust Diffusion

While turbulent motion of gas drives dust collisions, dust grains are also subject to turbulent diffusion that smooths out dust density perturbations. The diffusion is expected to suppress the coagulation instability, especially at short wavelengths, and it limits the growth rate. In this subsection, we discuss to what extent the diffusion suppresses the instability performing one-fluid analyses.

The dust diffusion is often modeled by a diffusion term introduced in the dust continuity equation. The form of the diffusive mass flux depends on a closure relation between turbulent fluctuations and mean-field components. The usually assumed diffusive mass flux is proportional to the gradient of either dust density or dust-to-gas ratio (e.g., Cuzzi et al. 1993; Dubrulle et al. 1995). However, simply adding the diffusion term to the continuity equation introduces unphysical momentum flux, which violates the total angular momentum conservation (Goodman & Pindor 2000; Tominaga et al. 2019). Tominaga et al. (2019) shows that replacing the dust velocity by the sum of the mean-flow velocity and the diffusive flux terms recovers the angular momentum conservation. The equations including such terms are mathematically and physically derived from the mean-field approximation of the usual momentum equations (see Appendix A in Tominaga et al. 2019). Following Tominaga et al. (2019) in order to discuss the effects of the diffusion, we simply replace v_x in Equations (1) and (58) by

$$v_x = \langle v_x \rangle - \frac{D}{\Sigma_d} \frac{\partial \Sigma_d}{\partial x}, \quad (64)$$

or

$$v_x = \langle v_x \rangle - \frac{D\Sigma_g}{\Sigma_d} \frac{\partial}{\partial x} \left(\frac{\Sigma_d}{\Sigma_g} \right). \quad (65)$$

where D is a diffusion coefficient and $\langle v_x \rangle$ is the mean-flow component representing the so-called drift and defined by

$$\langle v_x \rangle \equiv -\frac{2\tau_s}{1 + \tau_s^2} \eta R \Omega. \quad (66)$$

The resultant equations with Equation (64) are

$$\frac{\partial \Sigma_d}{\partial t} + \frac{\partial \Sigma_d \langle v_x \rangle}{\partial x} = \frac{\partial}{\partial x} \left(D \frac{\partial \Sigma_d}{\partial x} \right) \quad (67)$$

$$\begin{aligned} \frac{\partial \tau_s}{\partial t} + \left(\langle v_x \rangle - \frac{D}{\Sigma_d} \frac{\partial \Sigma_d}{\partial x} \right) \frac{\partial \tau_s}{\partial x} \\ = \frac{\Sigma_d}{\Sigma_g} \frac{\tau_s}{3t_0} - \frac{\tau_s}{\Sigma_g} \left(\langle v_x \rangle - \frac{D}{\Sigma_d} \frac{\partial \Sigma_d}{\partial x} \right) \frac{\partial \Sigma_g}{\partial x}. \end{aligned} \quad (68)$$

In the case we use Equation (65), we obtain the following equations:

$$\frac{\partial \Sigma_d}{\partial t} + \frac{\partial \Sigma_d \langle v_x \rangle}{\partial x} = \frac{\partial}{\partial x} \left(D \Sigma_g \frac{\partial}{\partial x} \left(\frac{\Sigma_d}{\Sigma_g} \right) \right) \quad (69)$$

$$\begin{aligned} \frac{\partial \tau_s}{\partial t} + \left(\langle v_x \rangle - \frac{D \Sigma_g}{\Sigma_d} \frac{\partial}{\partial x} \left(\frac{\Sigma_d}{\Sigma_g} \right) \right) \frac{\partial \tau_s}{\partial x} \\ = \frac{\Sigma_d}{\Sigma_g} \frac{\tau_s}{3t_0} - \frac{\tau_s}{\Sigma_g} \left(\langle v_x \rangle - \frac{D \Sigma_g}{\Sigma_d} \frac{\partial}{\partial x} \left(\frac{\Sigma_d}{\Sigma_g} \right) \right) \frac{\partial \Sigma_g}{\partial x}. \end{aligned} \quad (70)$$

We perform linear analyses based on Equations (67) and (68) and those based on Equations (69) and (70). In both cases, we set unperturbed states with uniform dust surface density and normalized stopping time, and take into account the dust growth equation (Equation (68) or (70)) only for perturbed quantities as in Sections 2 and 3.

First, we present results of the linear analyses with Equations (67) and (68). In this case, the unperturbed velocity $v_{x,0}$ is $v_{x,0} = \langle v_{x,0} \rangle = -2\tau_{s,0} R \Omega / (1 + \tau_{s,0}^2)$. Based on the above unperturbed state with uniform $\Sigma_{d,0}$ and $\tau_{s,0}$, we obtain the following linearized equations:

$$(n + ik \langle v_{x,0} \rangle + Dk^2) \frac{\delta \Sigma_d}{\Sigma_{d,0}} + \frac{1 - \tau_{s,0}^2}{1 + \tau_{s,0}^2} ik \langle v_{x,0} \rangle \frac{\delta \tau_s}{\tau_{s,0}} = 0, \quad (71)$$

$$\begin{aligned} \left(n + ik \langle v_{x,0} \rangle - \frac{\varepsilon}{3t_0} + \frac{2 \langle v_{x,0} \rangle \Sigma'_{g,0}}{1 + \tau_{s,0}^2 \Sigma_{g,0}} \right) \frac{\delta \tau_s}{\tau_{s,0}} \\ + \left(-\frac{\varepsilon}{3t_0} - ikD \frac{\Sigma'_{g,0}}{\Sigma_{g,0}} \right) \frac{\delta \Sigma_d}{\Sigma_{d,0}} = 0. \end{aligned} \quad (72)$$

The full dispersion relation is

$$(n + ik \langle v_{x,0} \rangle)^2 + A_1 (n + ik \langle v_{x,0} \rangle) + A_0 = 0, \quad (73)$$

$$A_1 = -\frac{\varepsilon}{3t_0} + \frac{2 \langle v_{x,0} \rangle \Sigma'_{g,0}}{1 + \tau_{s,0}^2 \Sigma_{g,0}} + Dk^2, \quad (74)$$

$$\begin{aligned} A_0 = ik \langle v_{x,0} \rangle \left(\frac{1 - \tau_{s,0}^2}{1 + \tau_{s,0}^2} \right) \left(\frac{\varepsilon}{3t_0} + ikD \frac{\Sigma'_{g,0}}{\Sigma_{g,0}} \right) \\ + Dk^2 \left(-\frac{\varepsilon}{3t_0} + \frac{2 \langle v_{x,0} \rangle \Sigma'_{g,0}}{1 + \tau_{s,0}^2 \Sigma_{g,0}} \right). \end{aligned} \quad (75)$$

The terms proportional to $\Sigma'_{g,0}$ originate from the last term on the right-hand side of Equation (68). Using $L_{\text{gdl}} = 3t_0 \langle v_{x,0} \rangle / \varepsilon$ and W defined by Equation (60), we obtain the dispersion

relation of a growing mode in the dimensionless form

$$\begin{aligned} n \left(\frac{3t_0}{\varepsilon} \right) = ik + \frac{1}{2} (W - \beta \tilde{k}^2) \\ + \frac{1}{2} \sqrt{(W + \beta \tilde{k}^2)^2 + 4ik \frac{1 - \tau_{s,0}^2}{1 + \tau_{s,0}^2} \left(1 + ik \beta L_{\text{gdl}} \frac{\Sigma'_{g,0}}{\Sigma_{g,0}} \right)}, \end{aligned} \quad (76)$$

where $\beta = DL_{\text{gdl}}^{-2} (3t_0/\varepsilon)$ is the diffusion coefficient normalized by the growth-drift length L_{gdl} and the dust coagulation timescale $3t_0/\varepsilon$. Assuming small dust particles ($\tau_{s,0} \ll 1$) and $D \simeq \alpha c_s^2 \Omega^{-1}$ (see Youdin & Lithwick 2007), we can relate β to α as follows (see also Equation (18)):

$$\begin{aligned} \beta \simeq \alpha \left(\frac{H}{L_{\text{gdl}}} \right)^2 \frac{3t_0 \Omega}{\varepsilon} \\ \simeq 1.7 \times 10^{-4} \left(\frac{\alpha}{1.0 \times 10^{-4}} \right) \left(\frac{t_0 \Omega}{0.50} \right)^{-1} \\ \times \left(\frac{\varepsilon}{1.0 \times 10^{-3}} \right) \left(\frac{|v_{x,0}|/c_s}{2.0 \times 10^{-2}} \right)^{-2}. \end{aligned} \quad (77)$$

We note that β depends on dust sizes since $|v_{x,0}|$ depends on $\tau_{s,0}$. To compare the simple and modified one-fluid analyses (see also Section 3.3), we calculate both (1) growth rates without the terms proportional to $\Sigma'_{g,0}$ and (2) growth rates with all terms in Equation (76).

Figure 7 shows the growth rates for $\tau_s = 0.1$. The color shows the growth rates normalized by the dust coagulation timescale $3t_0/\varepsilon$. The left panel shows the growth rate calculated without the last term proportional to $\Sigma'_{g,0}$ on the right-hand side of Equation (68), while the right panel shows the growth rate with all terms. We also assume $W = 1$ in the left panel. In both cases, the coagulation instability is stabilized by dust diffusion at short wavelengths. As a result, the coagulation instability has the most unstable wavenumber k_{max} in contrast to the diffusion-free case (Sections 2 and 3). We find that the most unstable wavenumber can be estimated well by the following relation when $|W|$ is not so large (~ 1):

$$k_{\text{max}} L_{\text{gdl}} \simeq \frac{1}{3} \left(\frac{4}{\beta^2} \frac{1 - \tau_{s,0}^2}{1 + \tau_{s,0}^2} \right)^{1/3}. \quad (78)$$

The dashed line in Figure 7 represents the wavenumber calculated with Equation (78). In both panels, Equation (78) well-represents the most unstable wavenumber. Considering small dust particles and adopting $1 \pm \tau_{s,0}^2 \simeq 1$, we obtain the most unstable wavelength $\lambda_{\text{max}} \equiv 2\pi/k_{\text{max}}$ as

$$\begin{aligned} \lambda_{\text{max}} \simeq 1.1H \left(\frac{\alpha}{1.0 \times 10^{-4}} \right)^{2/3} \left(\frac{t_0 \Omega}{0.50} \right)^{1/3} \\ \times \left(\frac{\varepsilon}{1.0 \times 10^{-3}} \right)^{-1/3} \left(\frac{|v_{x,0}|/c_s}{2.0 \times 10^{-2}} \right)^{-1/3}. \end{aligned} \quad (79)$$

As in the case without the dust diffusion (Section 3.3), including the effect of $\Sigma'_{g,0}$ in the dust growth equation reduces the growth rate by a factor of a few for $L_{\text{gdl}} \simeq 33.8H$ (see the right panel of Figure 7). When a gas disk is less turbulent and β becomes less than 1×10^{-4} , the coagulation instability grows 2–10 times faster than dust particles coagulate. Such a situation

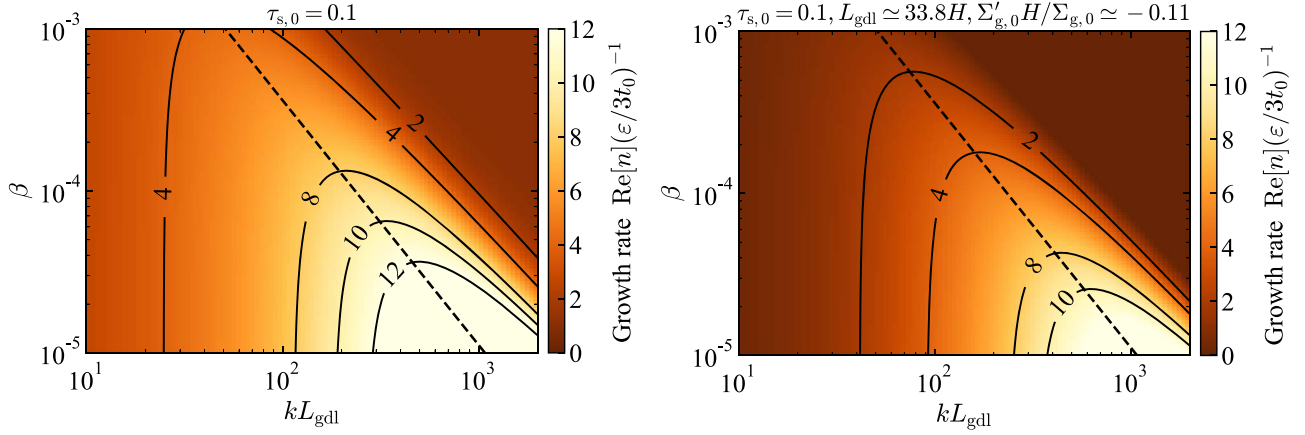


Figure 7. Growth rates in the cases with dust diffusion. In both panels, the horizontal axis is wavenumber normalized by the growth-drift length L_{gdl} , and the vertical axis is the dimensionless diffusivity $\beta = DL_{\text{gdl}}^{-2}(3t_0/\varepsilon)$. The left panel shows the growth rate calculated without the terms proportional to $\Sigma'_{\text{g},0}$ in Equation (76). The right panel shows the growth rate with all terms in Equation (76). In the presence of dust diffusion due to weak turbulence, growth rates of coagulation instability are larger than the dust growth rate $\varepsilon/3t_0$. Dashed lines in both panels show the wavenumber given by Equation (78). The most unstable wavenumber is described well by Equation (78).

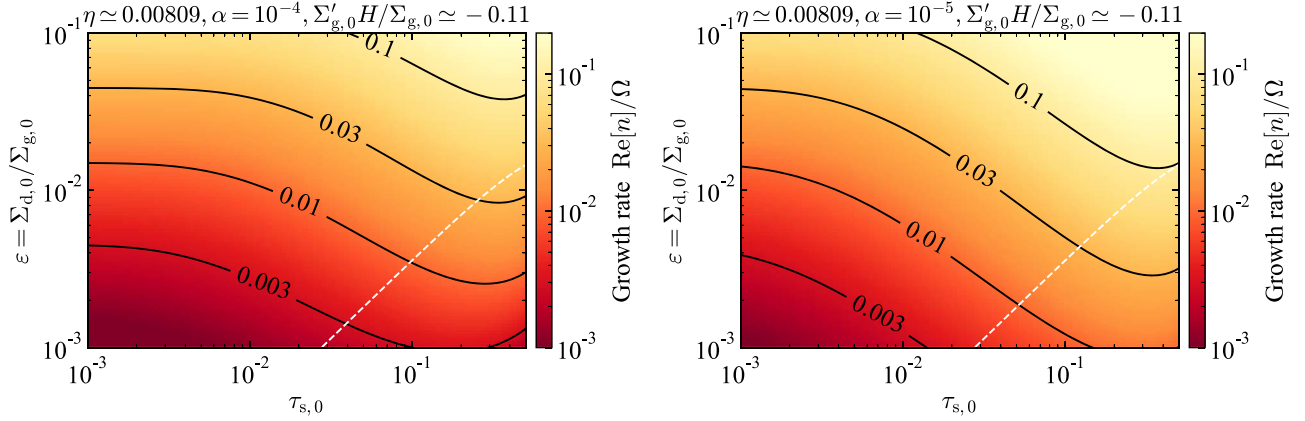


Figure 8. Growth rate with the dust diffusion (Equation (76)) in the unit of Ω at $kL_{\text{gdl}} = (4\beta^{-2}(1 - \tau_{\text{s},0}^2)/27(1 + \tau_{\text{s},0}^2))^{1/3}$ (Equation (78)) as a function of the normalized stopping time $\tau_{\text{s},0}$ and the unperturbed dust-to-gas surface density ratio $\varepsilon = \Sigma_{\text{d},0}/\Sigma_{\text{g},0}$. The left figure shows the growth rate for $\alpha = 10^{-4}$, and the right figure shows the growth rate for $\alpha = 10^{-5}$. The white dashed lines in both panels show sets of $(\tau_{\text{s},0}, \varepsilon)$ that satisfy $\Sigma_{\text{d},0}/3t_0 = \langle v_{\text{x},0} \rangle \Sigma'_{\text{g},0}$, meaning that the equation for τ_{s} is exactly satisfied in the steady unperturbed state with uniform $\tau_{\text{s},0}$ and $\Sigma_{\text{d},0}$, and thus our analysis is rigorous. For given $\tau_{\text{s},0}$ and ε , the growth rate of coagulation instability is larger for smaller α . Even for $\varepsilon \sim 10^{-3}$, the growth timescale $1/\text{Re}[n]$ can be a few tens of the orbital period ($2\pi/\Omega$) if dust particles are large and $\tau_{\text{s},0} \simeq 10^{-1}$.

is realized in a region where $\alpha \times \varepsilon \lesssim 6 \times 10^{-8}$ for $|v_{\text{x},0}|/c_{\text{s}} = 0.02$ (see Equation (77)).

Figure 8 shows growth rates in the unit of Ω calculated with Equations (76) and (78). Following Youdin & Lithwick (2007) and Youdin (2011), we calculate the diffusion coefficient as

$$D = \frac{1 + \tau_{\text{s},0} + 4\tau_{\text{s},0}^2}{(1 + \tau_{\text{s},0}^2)^2} \alpha c_{\text{s}} H. \quad (80)$$

The white dashed lines on both panels show sets of $(\tau_{\text{s},0}, \varepsilon)$ satisfying $\Sigma_{\text{d},0}/3t_0 = \langle v_{\text{x},0} \rangle \Sigma'_{\text{g},0}$. This means that the equation for τ_{s} (Equation (68)) is satisfied with uniform $\tau_{\text{s},0}$ and $\Sigma_{\text{d},0}$ in the steady unperturbed state. In other words, the adopted uniform state is not an approximated solution as explained in the beginning of Section 2.2, but rather an exact steady solution in the present one-fluid formalism. Thus, the present one-fluid analysis is rigorous on the white dashed lines. The strength of turbulence α is assumed to be 10^{-4} in the left panel of Figure 8,

and 10^{-5} in the right panel. In these cases, the coagulation instability can develop within a few tens of the orbital period even when the dust-to-gas ratio is less than 0.01. Because we use Equation (78) to obtain the approximated maximum growth rates in Figure 8, one finds not only β larger but also kL_{gdl} smaller for smaller $\tau_{\text{s},0}$. The long-wavelength limit ($kL_{\text{gdl}} \rightarrow 0$) gives the growth rate of $\varepsilon/3t_0$ as also discussed in Section 2. Note that small $\tau_{\text{s},0}$ makes $L_{\text{gdl}} \propto |v_{\text{x},0}|$ smaller, leading to $n \times (3t_0/\varepsilon) = W \rightarrow 1$ at $k=0$ as $\tau_{\text{s},0} \rightarrow 0$ (see also Equation (60)). This is the reason why the growth rate remains relatively constant at small $\tau_{\text{s},0}$ and depends on only ε in Figure 8.

Linear analyses with Equations (69) and (70) show little difference from the above analyses with Equations (67) and (68). We thus simply show a derived dispersion relation. The unperturbed state with uniform $\Sigma_{\text{g},0}$ has the dust drift velocity $v_{\text{x},0} = \langle v_{\text{x},0} \rangle + D\Sigma'_{\text{g},0}/\Sigma_{\text{g},0}$. Linearizing Equations (69) and (70),

we obtain the following dispersion relation:

$$(n + ikv_{x,0})^2 + B_1(n + ikv_{x,0}) + B_0 = 0, \quad (81)$$

$$B_1 = -\frac{\varepsilon}{3t_0} + \frac{2v_{x,0}}{1 + \tau_{s,0}^2} \frac{\Sigma'_{g,0}}{\Sigma_{g,0}} + Dk^2 - D \left(\frac{\Sigma'_{g,0}}{\Sigma_{g,0}} \right)^2 \frac{1 - \tau_{s,0}^2}{1 + \tau_{s,0}^2}, \quad (82)$$

$$B_0 = ikv_{x,0} \left(\frac{1 - \tau_{s,0}^2}{1 + \tau_{s,0}^2} \right) \left(\frac{\varepsilon}{3t_0} + ikD \frac{\Sigma'_{g,0}}{\Sigma_{g,0}} \right) + Dk^2 \left(-\frac{\varepsilon}{3t_0} + \frac{2v_{x,0}}{1 + \tau_{s,0}^2} \frac{\Sigma'_{g,0}}{\Sigma_{g,0}} \right) - \frac{ik\varepsilon D}{3t_0} \frac{\Sigma'_{g,0}}{\Sigma_{g,0}} \frac{1 - \tau_{s,0}^2}{1 + \tau_{s,0}^2}. \quad (83)$$

The differences from Equations (76)–(75) are twofold: (1) $\langle v_{x,0} \rangle$ is replaced with $v_{x,0}$, and (2) the last terms on the right-hand side of Equations (82) and (83). The former difference is small when $\tau_{s,0}$ is larger than α and $|\langle v_{x,0} \rangle| > D|\Sigma'_{g,0}/\Sigma_{g,0}|$. The latter difference is also small. Because the coagulation instability grows at $kH \gtrsim 1$ and $kR \gg 1$ in weakly turbulent disks, the last term of Equation (82) is much smaller than the third term Dk^2 . The last term on the right-hand side of Equation (83) is also small compared to the first term when $\tau_{s,0} > \alpha$ and $|v_{x,0}| > D|\Sigma'_{g,0}/\Sigma_{g,0}|$ are satisfied. Because of $H_d/H \simeq \sqrt{\alpha/\tau_{s,0}}$, the condition $\tau_{s,0} > \alpha$ is equivalent to $H_d < H$, which we usually expect.

4.2. Backreaction at the Midplane

In Section 2, we neglect the frictional backreaction to the gas and use the drift velocity of the test particle limit. In Section 3, we take into account the backreaction in the two-fluid height-integrated system, but the backreaction terms are proportional to the dust-to-gas surface density ratio. In reality, dust grains settle around the midplane and the backreaction is determined by the midplane dust-to-gas ratio ε_{mid} :

$$\varepsilon_{\text{mid}} \equiv \frac{H\Sigma_d}{H_d\Sigma_g} = \sqrt{\frac{\tau_s}{\alpha}} \varepsilon, \quad (84)$$

where we approximate the dust scale height with $H_d = H\sqrt{\alpha/\tau_s}$ (see also Appendix C for sublayer modeling). The midplane dust-to-gas ratio ε_{mid} is larger than $\varepsilon = \Sigma_d/\Sigma_g$ for small H_d/H , which brakes dust grains and can limit the efficiency of the traffic jam, and thus the coagulation instability.⁶ Moreover, the degree of dust settling depends on stopping time and thus is time-dependent and spatially dependent during the growth of coagulation instability. Therefore, in this subsection, utilizing one-fluid equations, we discuss coagulation instability under the radial drift mediated by the τ_s -dependent midplane dust-to-gas mass ratio ε_{mid} .

⁶ One could modify the backreaction terms in gas equations by multiplying a numerical factor of $\varepsilon_{\text{mid}}/\varepsilon$ to mimic the midplane backreaction in a full-disk averaging model. However, such a modeling will violate the conservation of momentum. Violation of the conservation law leads to unphysical mode properties, which is discussed in another context (diffusion modeling) in Tominaga et al. (2019). Thus, we only consider the dust motion and regard the gas as a momentum reservoir in this subsection. We describe another model based on a sublayer averaging in Appendix C.

The dust velocity is given by

$$\langle v_x \rangle = -\frac{2\tau_s}{(1 + \varepsilon_{\text{mid}})^2 + \tau_s^2} \eta R \Omega. \quad (85)$$

Taking into account the diffusion, we use Equations (67) and (68) in this subsection. We note that the coagulation rate is still determined by the dust-to-gas surface density ratio Σ_d/Σ_g regardless of the modification of the velocity with the midplane dust-to-gas ratio. Linearizing Equations (84) and (85) with $\Sigma_g = \Sigma_{g,0}$ gives

$$\frac{\delta\varepsilon_{\text{mid}}}{\varepsilon_{\text{mid},0}} = \frac{\delta\Sigma_d}{\Sigma_{d,0}} + \frac{1}{2} \frac{\delta\tau_s}{\tau_{s,0}}, \quad (86)$$

$$\frac{\delta\langle v_x \rangle}{\langle v_{x,0} \rangle} = \frac{1 + \varepsilon_{\text{mid},0} - \tau_{s,0}^2}{(1 + \varepsilon_{\text{mid},0})^2 + \tau_{s,0}^2} \frac{\delta\tau_s}{\tau_{s,0}} - \frac{2\varepsilon_{\text{mid},0}(1 + \varepsilon_{\text{mid},0})}{(1 + \varepsilon_{\text{mid},0})^2 + \tau_{s,0}^2} \frac{\delta\Sigma_d}{\Sigma_{d,0}}, \quad (87)$$

where $\varepsilon_{\text{mid},0} \equiv (\Sigma_{d,0}/\Sigma_{g,0})\sqrt{\tau_{s,0}/\alpha} = \varepsilon\sqrt{\tau_{s,0}/\alpha}$ and

$$\langle v_{x,0} \rangle = -\frac{2\tau_{s,0}}{(1 + \varepsilon_{\text{mid},0})^2 + \tau_{s,0}^2} \eta R \Omega. \quad (88)$$

One can derive a dispersion relation using Equation (87) and

$$(n + ik\langle v_{x,0} \rangle + Dk^2) \frac{\delta\Sigma_d}{\Sigma_{d,0}} + ik\delta\langle v_x \rangle = 0, \quad (89)$$

$$\begin{aligned} & \left(n + ik\langle v_{x,0} \rangle - \frac{\varepsilon}{3t_0} + \frac{\langle v_{x,0} \rangle \Sigma'_{g,0}}{\Sigma_{g,0}} \right) \frac{\delta\tau_s}{\tau_{s,0}} \\ & = \left(\frac{\varepsilon}{3t_0} + \frac{Dik\Sigma'_{g,0}}{\Sigma_{g,0}} \right) \frac{\delta\Sigma_d}{\Sigma_{d,0}} - \frac{\Sigma'_{g,0}}{\Sigma_{g,0}} \delta\langle v_x \rangle, \end{aligned} \quad (90)$$

which are the linearized equations of Equations (67) and (68), respectively. We obtain the following dispersion relation of coagulation instability

$$\begin{aligned} n \left(\frac{3t_0}{\varepsilon} \right) &= i\tilde{k} + \frac{1}{2} \left(W_{\text{mod}} - \beta\tilde{k}^2 - \frac{2i\tilde{k}\varepsilon_{\text{mid},0}(1 + \varepsilon_{\text{mid},0})}{(1 + \varepsilon_{\text{mid},0})^2 + \tau_{s,0}^2} \right) \\ &+ \frac{1}{2} \left[\left(W_{\text{mod}} + \beta\tilde{k}^2 + \frac{2i\tilde{k}\varepsilon_{\text{mid},0}(1 + \varepsilon_{\text{mid},0})}{(1 + \varepsilon_{\text{mid},0})^2 + \tau_{s,0}^2} \right)^2 \right. \\ &+ 4i\tilde{k} \frac{1 + \varepsilon_{\text{mid},0} - \tau_{s,0}^2}{(1 + \varepsilon_{\text{mid},0})^2 + \tau_{s,0}^2} \\ &\left. \times \left\{ 1 + L_{\text{gdl}} \frac{\Sigma'_{g,0}}{\Sigma_{g,0}} \left(i\tilde{k}\beta - \frac{2\varepsilon_{\text{mid},0}(1 + \varepsilon_{\text{mid},0})}{(1 + \varepsilon_{\text{mid},0})^2 + \tau_{s,0}^2} \right) \right\} \right]^{1/2}, \end{aligned} \quad (91)$$

where W_{mod} is given by

$$W_{\text{mod}} \equiv 1 + \frac{(1 + \varepsilon_{\text{mid},0})(2 + \varepsilon_{\text{mid},0}) L_{\text{gdl}} \Sigma'_{g,0}}{(1 + \varepsilon_{\text{mid},0})^2 + \tau_{s,0}^2} \frac{1}{\Sigma_{g,0}}. \quad (92)$$

As already discussed in Sections 3.3 and 4.1, W_{mod} and the terms proportional to $L_{\text{gdl}} \Sigma'_{g,0}/\Sigma_{g,0}$ represent the stabilizing effects due to the second term on the right-hand side of Equation (68). To focus on stabilizing effects due to the backreaction with ε_{mid} , we first set $W_{\text{mod}} = 1$ and neglect the other terms proportional to

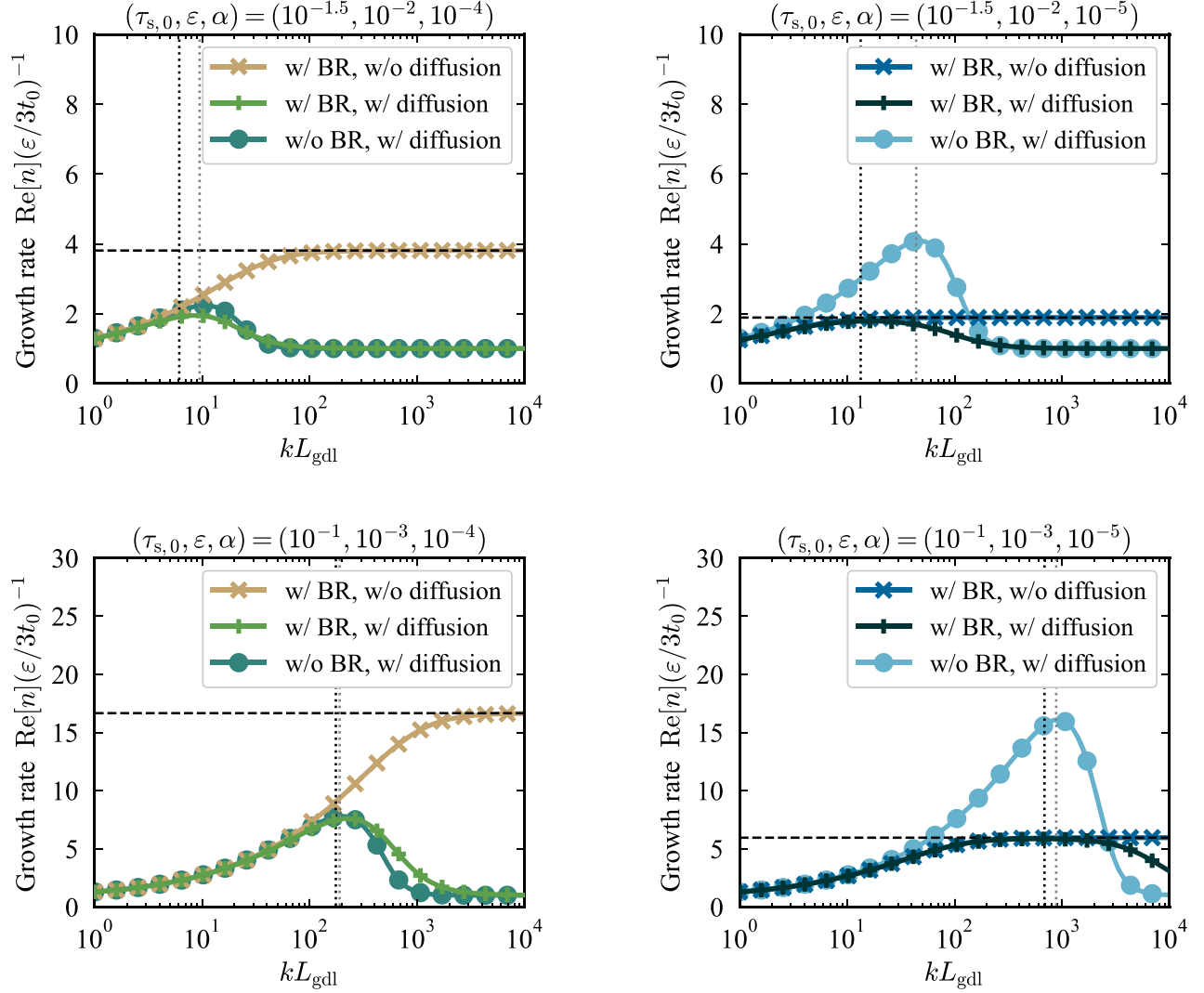


Figure 9. Growth rate obtained from Equation (93). The “BR” in the legends stands for backreaction calculated with the midplane dust-to-gas ratio ε_{mid} . Cross marks, plus marks, and filled circles show different growth rates and represent whether the backreaction or diffusion is considered or not. Each panel shows growth rates for different parameters: $(\tau_{s,0}, \varepsilon, \alpha)$. The top panels and the bottom panels are results of $(\tau_{s,0}, \varepsilon) = (10^{-1.5}, 10^{-2})$ and $(10^{-1}, 10^{-3})$, respectively. We use $\alpha = 10^{-4}$ for the left column and $\alpha = 10^{-5}$ for the right column. The black dashed line shows the upper limit of the growth rate given by Equation (94). In the presence of the diffusion, the maximum growth rates are similar to those obtained in the absence of the backreaction (see the left column), or limited by the black dashed line (see the right column). The black and gray vertical dotted lines represent wavelengths estimated from Equation (78) for the cases with and without the backreaction, respectively. We note that β is changed by the inclusion of the backreaction because the drift velocity is reduced. The estimated wavenumbers (the black dotted lines) match the most unstable wavenumbers within errors of a few tens of percent in the four panels. Therefore, Equation (78) can be used for rough estimation of the most unstable wavenumber in the present analyses with the backreaction.

$L_{\text{gdl}} \Sigma'_{\text{g},0} / \Sigma_{\text{g},0}$. Thus, the dispersion relation discussed below is

$$\begin{aligned}
 n\left(\frac{3t_0}{\varepsilon}\right) &= i\tilde{k} + \frac{1}{2} \left(1 - \beta\tilde{k}^2 - \frac{2i\tilde{k}\varepsilon_{\text{mid},0}(1 + \varepsilon_{\text{mid},0})}{(1 + \varepsilon_{\text{mid},0})^2 + \tau_{s,0}^2} \right) \\
 &+ \frac{1}{2} \left[\left(1 + \beta\tilde{k}^2 + \frac{2i\tilde{k}\varepsilon_{\text{mid},0}(1 + \varepsilon_{\text{mid},0})}{(1 + \varepsilon_{\text{mid},0})^2 + \tau_{s,0}^2} \right)^2 \right. \\
 &\left. + 4i\tilde{k} \frac{1 + \varepsilon_{\text{mid},0} - \tau_{s,0}^2}{(1 + \varepsilon_{\text{mid},0})^2 + \tau_{s,0}^2} \right]^{1/2}. \quad (93)
 \end{aligned}$$

The parameters determining the growth rates are $\tau_{s,0}$, ε , and α . The midplane dust-to-gas ratio $\varepsilon_{\text{mid},0}$ is determined by those parameters through Equation (84).

Figure 9 shows growth rates for four different parameter sets: $(\tau_{s,0}, \varepsilon, \alpha) = (10^{-1.5}, 10^{-2}, 10^{-4})$, $(10^{-1.5}, 10^{-2}, 10^{-5})$, $(10^{-1}, 10^{-3}, 10^{-4})$, and $(10^{-1}, 10^{-3}, 10^{-5})$. Each panel shows three dispersion relations whose difference is whether the backreaction and diffusion are included or not. The left column shows the results for $\alpha = 10^{-4}$. In the absence of the diffusion, the growth rate is independent from wavenumbers at $kL_{\text{gdl}} > 10^2$ for the left top panel and $kL_{\text{gdl}} > 10^3$ for the left bottom panel, respectively. In other words, a combined effect

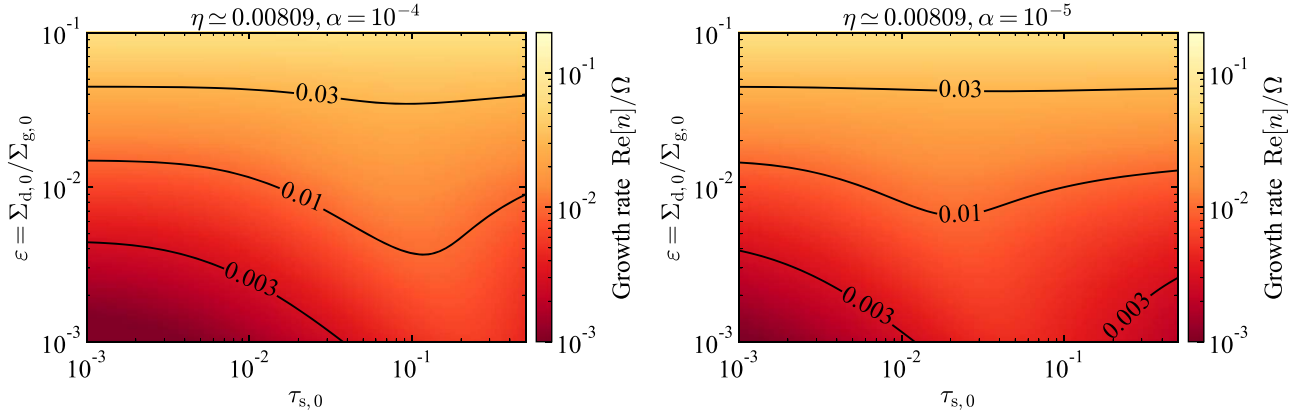


Figure 10. Maximum growth rates with the effect of backreaction (Equation (93)) as a function of the normalized stopping time $\tau_{s,0}$ and the unperturbed dust-to-gas surface density ratio $\varepsilon = \Sigma_{d,0}/\Sigma_{g,0}$. The left figure shows the growth rate for $\alpha = 10^{-4}$, and the right figure shows the growth rate for $\alpha = 10^{-5}$. The reduction of the growth rates is less significant for $\alpha = 10^{-4}$ than for $\alpha = 10^{-5}$. The reduction is also less significant for smaller $\tau_{s,0}$ (e.g., $\tau_{s,0} \lesssim 0.1$ in the left panel).

of τ_s -dependent midplane dust-gas ratio and the deceleration due to the backreaction limits the growth of coagulation instability. Equation (93) with $\beta = 0$ is reduced at $\varepsilon_{\text{mid},0}^2 \tilde{k} \gg 1$ as follows

$$n\left(\frac{3t_0}{\varepsilon}\right) \simeq i\tilde{k} + \frac{1}{2} \left(1 + \frac{(1 + \varepsilon_{\text{mid},0})^2 - \tau_{s,0}^2}{\varepsilon_{\text{mid},0}(1 + \varepsilon_{\text{mid},0})} \right) + \frac{i}{\tilde{k}} \frac{((1 + \varepsilon_{\text{mid},0})^4 - \tau_{s,0}^4)((1 + \varepsilon_{\text{mid},0})^2 - \tau_{s,0}^2)}{8\varepsilon_{\text{mid},0}^3(1 + \varepsilon_{\text{mid},0})^3}. \quad (94)$$

The upper limit of the growth rate is given by the second term on the right-hand side, which is shown by dashed lines in Figure 9.

The growth rates in the presence of the diffusion are shown by plus marks and filled circles in Figure 9. In the left two panels, the diffusion significantly stabilizes coagulation instability, and the growth rate is smaller than the maximum growth rate shown by the black dashed line (Equation (94)) even in the absence of the backreaction. In those cases, including the backreaction insignificantly affects the maximum growth rates. On the other hand, the right two panels show larger growth rates in the absence of the backreaction (see filled circles) because the diffusion is ineffective. In this case, the backreaction limits the growth rates at larger kL_{gdI} , and the maximum growth rates are reproduced well by the black dashed line.

At wavenumbers larger than the most unstable wavenumber, the growth rate is slightly increased by the backreaction in the presence of the dust diffusion (see the plus marks and filled circles). This trend is more prominent in the lower two panels in Figure 9. We find that this increase originates from a cross term of $\beta \tilde{k}^2$ and $2i\tilde{k}\varepsilon_{\text{mid},0}(1.0 + \varepsilon_{\text{mid},0})/((1.0 + \varepsilon_{\text{mid},0})^2 + \tau_{s,0}^2)$ in the square root of the dispersion relation (see Equations (91) and (93)). The physical interpretation may be as follows. Including the dust diffusion can be regarded as modification in the velocity perturbation δv_x by $-ikD\delta\Sigma_d/\Sigma_{d,0} \propto \exp(-i\pi/2)\delta\Sigma_d$ as represented in Equation (64). Including the backreaction also modifies δv_x by the term proportional to $-2\varepsilon_{\text{mid},0}\langle v_{x,0} \rangle \delta\Sigma_d/\Sigma_{d,0}$ (see Equation (87)). Because coagulation instability in the absence of diffusion and backreaction has a phase difference of $3\pi/4$ between $\delta\Sigma_d$ and δv_x (see Equations (11) and (17)), the above two modifications act as a phase shift of δv_x in the opposite direction and cancel each other.

The black and gray vertical dotted lines in the four panels represent wavenumbers estimated by Equation (78). Note that β on the right-hand side of Equation (78) is changed by the inclusion of the backreaction because the drift velocity is reduced (see Equation (77)). The cases with the backreaction show the larger β and smaller wavenumber given by Equation (78). The black dotted lines match the most unstable wavenumbers within errors of a few tens of percent. Therefore, we can use Equation (78) for the rough estimation of $k_{\text{max}}L_{\text{gdI}}$.

As in Figure 8, we also plot the maximum growth rate as a function of $\tau_{s,0}$ and ε in the presence of backreaction. For simplicity and clarity, we first show the growth rates derived without the $\Sigma'_{g,0}$ and with $W_{\text{mod}} = 1$ (Equation (93)). Figure 10 shows the results for $\alpha = 10^{-4}$ (in the left panel) and $\alpha = 10^{-5}$ (in the right panel). In contrast to the previous sections, we numerically derive the maximum growth rate and the most unstable wavenumber instead of using Equation (78) for comparison with the case of nonzero $\Sigma'_{g,0}$ (see below). In most of the parameter space, the backreaction makes the growth rates only a few times smaller. The growth rates with $\alpha = 10^{-5}$ are smaller than those with $\alpha = 10^{-4}$ because weaker turbulence results in a denser midplane dust layer and makes the backreaction more effective. In a region of lower dust-to-gas ratio (e.g., $\Sigma_{d,0}/\Sigma_{g,0} \sim 10^{-3}$), the reduction of the growth rates is less significant than in a region of higher dust-to-gas ratio. The reduction is also less significant for smaller dust sizes, especially for the case of $\alpha = 10^{-4}$ (e.g., $\tau_{s,0} \lesssim 0.1$).

Next, we show the maximum growth rates with all the stabilizing effects including the gas surface density gradient (Equation (91)). We found that the most unstable wavenumber can deviate from the wavelength given by Equation (78) when W_{mod} is negative and $|W_{\text{mod}}|$ is relatively large. Thus, we numerically derive the most unstable wavelength instead of using the approximated formula. Figure 11 shows the results for $\alpha = 10^{-4}$ (in the left panel) and $\alpha = 10^{-5}$ (in the right panel). Comparing the derived growth rates with those in Figure 8, we find that the stabilizing effect due to the backreaction is insignificant for $\tau_{s,0} \lesssim 10^{-1}$ and $\varepsilon \lesssim 10^{-2}$, especially in the case of $\alpha = 10^{-4}$. One can see the stabilizing effect due to the gas surface density gradient by comparing Figures 10 and 11. The maximum growth rates become 0 in the white region in Figure 11. Including the gas gradient stabilizes the coagulation instability the most significantly for larger $\tau_{s,0}$ and smaller ε . According to the definition of W_{mod}

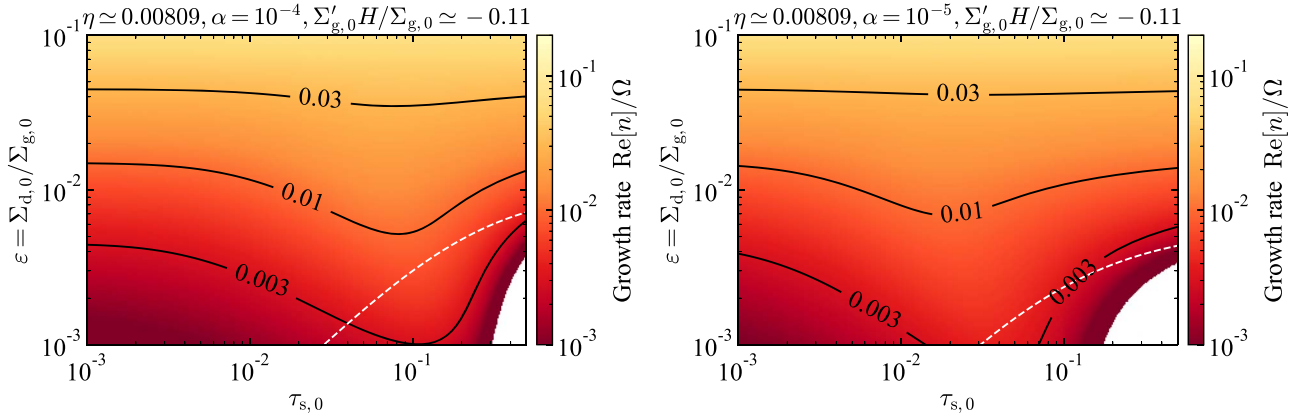


Figure 11. Maximum growth rates with all the stabilizing effects (Equation (91)). The left figure shows the growth rate for $\alpha = 10^{-4}$, and the right figure shows the growth rate for $\alpha = 10^{-5}$. The white dashed lines on both panels show sets of $(\tau_{s,0}, \varepsilon)$ that satisfy $\Sigma_{d,0}/3t_0 = \langle v_{x,0} \rangle \Sigma'_{g,0}$, meaning that the equation for τ_s is exactly satisfied in the steady unperturbed state with uniform $\tau_{s,0}$ and $\Sigma_{d,0}$, and thus our analysis is rigorous. Comparing with Figures 8 and 10, we find the growth rate with $\alpha = 10^{-4}$ to be similar for $\tau_{s,0} \lesssim 10^{-1}$ and $\varepsilon \lesssim 10^{-2}$. This trend can be also found on the right panel (i.e., $\alpha = 10^{-5}$). In the white regions in both panels, the coagulation instability is stable and the maximum value of $\text{Re}[n]$ is 0. The area of the white regions are relatively small in the plotted parameter space. Therefore, we expect that the coagulation instability can grow in most cases.

(Equation (92)), a combination of large $\tau_{s,0}$ and small ε leads to negative W_{mod} with its large magnitude, which stabilizes the instability. We find that the boundary between the colored and white regions in Figure 11 is approximately given by the following function F_{CI} :

$$\begin{aligned}
 F_{\text{CI}} \equiv & -\varepsilon_{\text{mid},0}^2(1 + \varepsilon_{\text{mid},0})^2 \\
 & + W_{\text{mod}}^{-2} \left((1 + \varepsilon_{\text{mid},0})^2 - \tau_{s,0}^2 + L_{\text{gdI}} \frac{\Sigma'_{g,0}}{\Sigma_{g,0}} \right. \\
 & \left. \times \frac{\varepsilon_{\text{mid},0}(1 + \varepsilon_{\text{mid},0})(\varepsilon_{\text{mid},0}^2 + \varepsilon_{\text{mid},0} + 2\tau_{s,0}^2)}{(1 + \varepsilon_{\text{mid},0})^2 + \tau_{s,0}^2} \right)
 \end{aligned} \quad (95)$$

Figure 12 shows F_{CI} normalized by $\sqrt{|F_{\text{CI}}|}$ as a function of $\tau_{s,0}$ and ε for $\alpha = 10^{-4}$. The value of F_{CI} is maximized for $W_{\text{mod}} = 0$, which can be seen as a color-saturated curve in the region of the bottom half. One can see that a region of $F_{\text{CI}} < 0$ matches with the stable region shown on the left panel of Figure 11.⁷ From Equation (95), we can also confirm that large $|W_{\text{mod}}|$ stabilizes the instability because the second term in Equation (95) decreases and F_{CI} becomes negative.

As above, we found the stabilization of the coagulation instability by the backreaction and the combination of the backreaction and the gas surface density gradient. We also found that a combination of diffusion and the gas surface density gradient stabilizes the instability for a much smaller dust-to-gas ratio ($\varepsilon \lesssim 10^{-4}$). Nevertheless, the stabilized region is limited in the plotted parameter region of Figure 11 ($\varepsilon \geq 10^{-3}$). Besides, the stabilization is insignificant in a dust-depleted region ($\varepsilon \sim 10^{-3}$) unless the dust size is not so large (e.g., $\tau_{s,0} \lesssim 0.1$). The previous studies on dust coagulation in protoplanetary disks show that dust-to-gas ratio decreases as dust grows in size. The dust depletion prevents $\tau_{s,0}$ from becoming large. This indicates that the growth condition of the

coagulation instability will be naturally satisfied. Therefore, we expect that coagulation instability can operate even when one considers the deceleration due to high dust-to-gas ratio at the midplane.

4.3. Effects of Enhanced Collision Velocities

Although we consider turbulence-induced collisions in the previous sections, the collision velocity in reality is determined by multiple components:

$$\Delta v_{\text{pp}} = \sqrt{(\Delta v_t)^2 + (\Delta v_B)^2 + (\Delta v_r)^2 + (\Delta v_\phi)^2 + (\Delta v_z)^2}, \quad (96)$$

where Δv_t is the turbulence-induced velocity, Δv_B is the collision velocity due to Brownian motion, and Δv_r , Δv_ϕ , and Δv_z are the relative velocities due to drift motion in the radial, azimuthal, and vertical directions, respectively. The coagulation instability is expected to have growth rates larger than those obtained in the Sections 2 and 3 because the coagulation timescale becomes shorter for a collision velocity larger than Δv_t .

We estimate how much the coagulation instability will be accelerated. For a collision of particles with masses of m_1 and m_2 , Δv_B is given by $\sqrt{8k_B T(m_1 + m_2)}/\pi m_1 m_2$, where k_B is the Boltzmann constant. Because collisional growth due to Brownian motion is effective for very small particles that are subject to insignificant drift (Brauer et al. 2008), we can neglect Δv_B for the coagulation instability, which requires significant drift. In the absence of backreaction from dust to gas, the radial, azimuthal, and vertical drift velocities of one dust particle are as follows (Nakagawa et al. 1986):

$$v_r(\tau_s) = -\frac{2\tau_s}{1 + \tau_s^2} \eta R \Omega \quad (97)$$

$$v_\phi(\tau_s) = R \Omega - \frac{1}{1 + \tau_s^2} \eta R \Omega, \quad (98)$$

$$v_z(\tau_s) = -\frac{\tau_s}{1 + \tau_s} z \Omega. \quad (99)$$

⁷ One can analytically derive the stability condition ($F_{\text{CI}} < 0$) from Equation (91) by seeking the condition that the growth rate is a decreasing function of k at $k \ll 1$ and assuming $\beta k^2 \ll 1$.

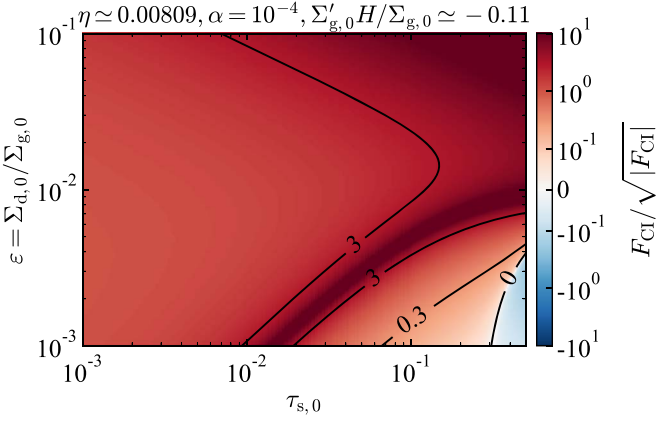


Figure 12. This figure shows F_{Ci} normalized by the square root of its magnitude as a function of $\tau_{s,0}$ and ε for $\alpha = 10^{-4}$. The blue region shows a region of $F_{Ci} < 0$, which matches with the stable region shown in the left panel of Figure 11.

Note that $v_r(\tau_s)$ refers to the velocity of a dust particle while v_x given by Equation (2) refers to the ensemble-averaged velocity derived from the vertically integrated equations. Because the moment equation tested by Sato et al. (2016) (Equation (4)) assumes collisions of particles whose size ratio is 0.5, the relative velocities due to drift motion are

$$|\Delta v_r| = \left| \frac{2 - \tau_s^2}{4 + \tau_s^2} v_r(\tau_s) \right|, \quad (100)$$

$$|\Delta v_\phi| = \frac{3\tau_s^2}{(4 + \tau_s^2)(1 + \tau_s^2)} \eta R \Omega \quad (101)$$

$$|\Delta v_z| = \frac{1}{2 + \tau_s} |v_z(\tau_s)|. \quad (102)$$

Assuming $\Delta v_t = \sqrt{C\alpha\tau_s}c_s$, one finds $\Delta v_r/\Delta v_t \propto \Delta v_z/\Delta v_t \propto \sqrt{\tau_s/\alpha}$ and $\Delta v_\phi/\Delta v_t \propto \tau_s\sqrt{\tau_s/\alpha}$ for a leading-order term. Because of such a τ_s -dependence, Δv_r and Δv_z dominate over Δv_ϕ for $\tau_s < 1$, and we may approximate the collision velocity Δv_{pp} with the following equation:

$$\Delta v_{pp} \simeq \Delta v_t \sqrt{1 + f \frac{\tau_s}{\alpha}}, \quad (103)$$

where f is defined as

$$\begin{aligned} f &\equiv \frac{\alpha}{\tau_s} \left(\left(\frac{\Delta v_r}{\Delta v_t} \right)^2 + \left(\frac{\Delta v_z}{\Delta v_t} \right)^2 \right), \\ &= \frac{4}{C} \left(\frac{2 - \tau_s^2}{(4 + \tau_s^2)(1 + \tau_s^2)} \right)^2 \left(\frac{\eta R \Omega}{c_s} \right)^2 \\ &\quad + \frac{1}{C(2 + \tau_s)^2(1 + \tau_s^2)} \left(\frac{z}{H} \right)^2, \end{aligned} \quad (104)$$

$$\simeq \frac{1}{C} \left[\left(\frac{\eta R \Omega}{c_s} \right)^2 + \left(\frac{z}{2H} \right)^2 \right]. \quad (105)$$

In the last equality, we make use of $\tau_s \ll 1$.

Substituting Equation (103) into Equation (8), we obtain

$$\frac{\partial \tau_s}{\partial t} + v_x \frac{\partial \tau_s}{\partial x} = \frac{\sqrt{\pi}}{4} \left(\frac{\Delta v_t}{\tau_s H_d} \right) \sqrt{1 + f \frac{\tau_s}{\alpha}} \frac{\Sigma_d}{\Sigma_{g,0}} \tau_s. \quad (106)$$

When turbulent motion determines the dust scale height and we can approximate $H_d \simeq \sqrt{\alpha/\tau_s}H$, Equation (106) is reduced to

$$\frac{\partial \tau_s}{\partial t} + v_x \frac{\partial \tau_s}{\partial x} = \sqrt{1 + f \frac{\tau_s}{\alpha}} \frac{\Sigma_d}{\Sigma_{g,0}} \frac{\tau_s}{3t_0}. \quad (107)$$

In this case, we can roughly expect that growth rates of the coagulation instability increase by $\sqrt{1 + f\tau_s/\alpha}$. We should note that the moment equation is derived from the vertically integrated coagulation equation (see Sato et al. 2016). Thus, the enhancement factor $\sqrt{1 + f\tau_s/\alpha}$ should be vertically averaged because Δv_z depends on z . Assuming the Gaussian profile for the vertical dust distribution, one finds the vertical collision rate can be expressed in terms of $\Delta v_z(z \sim H_d)$.⁸ Thus, we just take $z = H_d \simeq \sqrt{\alpha/\tau_s}H$ to evaluate Δv_z rather than exactly integrating and taking the vertical average of the enhancement factor. We then obtain $\sqrt{1 + f\tau_s/\alpha} \simeq 2.5$ for $\tau_s,0 = 0.1$, $\alpha = 10^{-4}$, $C = 2.3$, and $\eta R \Omega = 0.11c_s$, which corresponds to a value at $R = 20$ au in the minimum-mass solar nebula.

When gas turbulence is sufficiently weak, the dust scale height is determined by the settling motion. If the vertical relative velocity dominates over the other components, i.e., $\Delta v_{pp} \simeq \Delta v_z$, we expect $\Delta v_{pp}/\tau_s H_d \sim \Omega$, where we substitute $z = H_d$ to calculate Δv_z (see Nakagawa et al. 1981). In this case, Equation (106) is reduced to

$$\frac{\partial \tau_s}{\partial t} + v_x \frac{\partial \tau_s}{\partial x} \sim \frac{\sqrt{\pi}}{4} \frac{\Sigma_d}{\Sigma_{g,0}} \Omega \tau_s = \frac{\Sigma_d}{\Sigma_{g,0}} \frac{\tau_s}{3\sqrt{C}t_0}. \quad (108)$$

The growth rate of coagulation instability in this case is comparable to that expected in Section 2 because of $\sqrt{C} \simeq 1.5$. Including the radial relative velocity in Δv_{pp} gives

$$\frac{\partial \tau_s}{\partial t} + v_x \frac{\partial \tau_s}{\partial x} \sim \sqrt{1 + \left(\frac{\Delta v_r}{\Delta v_z} \right)^2} \frac{\Sigma_d}{\Sigma_{g,0}} \frac{\tau_s}{3\sqrt{C}t_0} \quad (109)$$

$$\sim \sqrt{1 + \left(\frac{2\eta R}{H_d} \right)^2} \frac{\Sigma_d}{\Sigma_{g,0}} \frac{\tau_s}{3\sqrt{C}t_0}. \quad (110)$$

Thus, we may expect larger growth rates by a factor of $\sim \sqrt{1 + 4\eta^2 R^2/H_d^2}$.

The present analyses describe the disk evolution with the height-integrated equations. We thus evaluate Δv_z adopting the representative height ($z \sim H_d$). To consider the vertical structure and dust motion might be important for more precise discussion on coagulation instability, because of the z -dependence of the collision velocity. Our future work will address this issue.

⁸ Using the Gaussian function for the vertical dust density, one can calculate the vertically averaged collision velocity due to the dust settling $\overline{\Delta v_z}$. Assuming that τ_s and Ω are almost constant within $|z| < H_d$, we obtain the approximated velocity $\overline{\Delta v_z} = \Delta v_z(z = \sqrt{2/\pi}H_{d,12})$ for a collision of dust grains with $\tau_s = \tau_{s,1}$ and $\tau_{s,2}$, where $H_{d,12} \equiv (H_d(\tau_{s,1})^{-2} + H_d(\tau_{s,2})^{-2})^{-1/2}$ (see Taki et al. 2021).

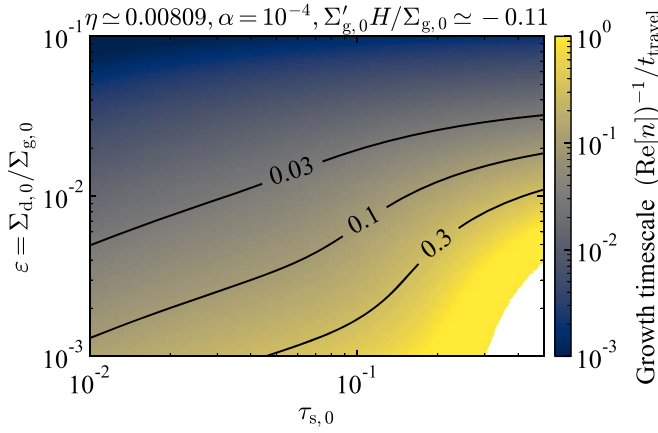


Figure 13. Growth timescale of the coagulation instability (Equation (91)) normalized by the traveling timescale of perturbations t_{travel} . We numerically find the shortest growth timescale as in Figure 11. The horizontal and vertical axes are the normalized stopping time $\tau_{s,0}$ and the unperturbed dust-to-gas surface density ratio $\varepsilon = \Sigma_{d,0}/\Sigma_{g,0}$, respectively. The strength of turbulence is assumed to be $\alpha = 10^{-4}$. The growth timescale is basically shorter than the traveling time except for the white region where the growth rate becomes 0. Thus, we expect that the coagulation instability develops before perturbations reach the central star.

4.4. Growth versus Drift

Perturbations growing via the coagulation instability travel inward with phase velocity $-\text{Im}[n]/k$ (see the left panels of Figures 4 and 5). The coagulation instability plays a significant role in disk evolution when the growth timescale of the instability is shorter than the timescale on which perturbations reach the central star. In this subsection, we examine whether the coagulation instability can grow significantly in a disk or not.

Although the phase velocity slightly deviates from dust drift velocity $v_{x,0}$ depending on wavelengths, we use $v_{x,0}$ to evaluate the traveling time of perturbations:

$$t_{\text{travel}} \equiv \frac{R}{|v_{x,0}|} = \frac{(1 + \varepsilon_{\text{mid}})^2 + \tau_s^2}{2\tau_{s,0}\eta\Omega}, \quad (111)$$

where we use the drift velocity mediated by the midplane dust-to-gas ratio. From this equation, we obtain $t_{\text{travel}}(2\pi/\Omega)^{-1} \simeq 100$ for $\tau_{s,0} = 0.1$, $\varepsilon_{\text{mid}} \ll 1$, and $\eta = 0.008$. Thus, perturbations reach a central star within one hundred orbital periods. Figure 13 shows growth timescale of the instability normalized by t_{travel} as a function of dust-gas ratio $\varepsilon = \Sigma_{d,0}/\Sigma_{g,0}$ and normalized stopping time $\tau_{s,0}$. We use Equation (91) to calculate the growth rate in Figure 13. The growth timescale is shorter than the traveling timescale in most of the plotted region. Although the growth timescale relative to the traveling timescale decreases as dust grains grow ($\tau_{s,0} \sim 0.1$), the growth timescale can be still three times shorter than the traveling timescale.

Because the growth rate just represents the e -folding time of perturbation amplitudes, it generally takes multiple times of the growth timescale for perturbations to grow significantly and develop into the nonlinear stage. The required time for perturbations to grow into nonlinear stage t_{nonlin} is represented in terms of initial amplitudes $\delta\Sigma_{d,\text{ini}}$ and amplitudes at

nonlinear stage $\delta\Sigma_d(t_{\text{nonlin}})$ as follows:

$$t_{\text{nonlin}} = \frac{\ln(\delta\Sigma_d(t_{\text{nonlin}})/\delta\Sigma_{d,\text{ini}})}{\text{Re}[n]}. \quad (112)$$

For significant growth of the coagulation instability, the timescale t_{nonlin} should be shorter than the traveling timescale t_{travel} . We can expect nonlinearity for $\delta\Sigma_d(t_{\text{nonlin}}) \sim \Sigma_{d,0}$. Therefore, t_{nonlin} is roughly given by

$$\begin{aligned} t_{\text{nonlin}} &\sim \frac{\ln(\Sigma_{d,0}/\delta\Sigma_{d,\text{ini}})}{\text{Re}[n]}, \\ &\simeq 2.3 \text{Re}[n]^{-1} \left(\frac{\ln(\Sigma_{d,0}/\delta\Sigma_{d,\text{ini}})}{\ln(10)} \right). \end{aligned} \quad (113)$$

When the initial amplitudes are 10% of $\Sigma_{d,0}$, t_{nonlin} becomes 2.3 times larger than the growth timescale, which satisfies the condition $t_{\text{nonlin}} < t_{\text{travel}}$ in most of the parameter space shown in Figure 13. An initial amplitude of 1% gives $t_{\text{nonlin}} \sim 4.6 \text{Re}[n]^{-1}$ and still satisfies the condition in most parameters ($\tau_{s,0}$, ε) shown in Figure 13.

4.5. Effects of Imperfect Sticking and Fragmentation

In the previous sections, we assume perfect sticking through particle collisions. Dust particles, however, experience imperfect sticking or fragment when collision speed becomes close to or larger than a critical speed, respectively (e.g., Wada et al. 2009, 2013). Erosive collisions also result in a decrease in the peak mass (Krijt et al. 2015).

We test if coagulation instability operates in the presence of imperfect sticking and collisional fragmentation. We modify Equation (9) by introducing a sticking efficiency p_{eff} as in previous studies (e.g., Okuzumi & Hirose 2012; Okuzumi et al. 2016; Ueda et al. 2019):

$$\frac{\partial \tau_s}{\partial t} + v_x \frac{\partial \tau_s}{\partial x} = p_{\text{eff}} \frac{\Sigma_d}{\Sigma_{g,0}} \frac{\tau_s}{3t_0}. \quad (114)$$

The previous works prescribe the sticking efficiency p_{eff} by fitting data of collision simulations of Wada et al. (2009) (e.g., see Figure 11 therein):

$$p_{\text{eff}} = \min \left(1, -\frac{\ln(\Delta v_{\text{pp}}/v_{\text{frag}})}{\ln 5} \right), \quad (115)$$

where v_{frag} denotes a critical fragmentation velocity (e.g., see Equation (12) in Ueda et al. 2019). We refer to imperfect sticking as a process of $0 \leq p_{\text{eff}} < 1$ and fragmentation as a process of $p_{\text{eff}} < 0$. In this study, we just formally show how the growth rates change because of p_{eff} .

We obtain the dispersion relation by replacing t_0 with t_0/p_{eff} in Equation (13):

$$\begin{aligned} n_{\text{ap},\pm} &\equiv -ikv_{x,0} \\ &+ p_{\text{eff}} \frac{\varepsilon}{6t_0} \left(1 \pm \sqrt{1 - p_{\text{eff}}^{-1} \frac{12t_0}{\varepsilon} \frac{1 - \tau_{s,0}^2}{1 + \tau_{s,0}^2} ikv_{x,0}} \right). \end{aligned} \quad (116)$$

⁹ The previous studies use ϵ_{eff} to denote the sticking efficiency (Okuzumi et al. 2016; Ueda et al. 2019). Because we already use similar variables, ε and ε_{mid} , to denote the dust-gas ratios, we use p_{eff} to avoid confusion.

When dust particles are subject to imperfect sticking ($0 < p_{\text{eff}} < 1$), the growth rate of coagulation instability decreases and is proportional to $\sqrt{p_{\text{eff}}}$ at short wavelengths.

In the case of fragmentation ($p_{\text{eff}} < 0$), we find that a mode with complex growth rate $n_{\text{ap},-}$ becomes unstable while the coagulation instability is stable (i.e., $\text{Re}[n_{\text{ap},+}] < 0$). The growth rate $\text{Re}[n_{\text{ap},-}]$ at short wavelengths is

$$\text{Re}[n_{\text{ap},-}] \simeq |p_{\text{eff}}| \frac{\varepsilon}{6t_0} \sqrt{\left| p_{\text{eff}}^{-1} \frac{6t_0}{\varepsilon} \frac{1 - \tau_{s,0}^2}{1 + \tau_{s,0}^2} k |v_{x,0}| \right|}. \quad (117)$$

At short wavelengths, relative amplitude of $\delta\tau_s$ and $\delta\Sigma_d$ is approximately given as

$$\frac{\delta\tau_s/\tau_{s,0}}{\delta\Sigma_d/\Sigma_{d,0}} \simeq -\exp\left(i\frac{\pi}{4}\right) \sqrt{\frac{|p_{\text{eff}}|\varepsilon}{3t_0k|v_{x,0}|} \frac{1 + \tau_{s,0}^2}{1 - \tau_{s,0}^2}}. \quad (118)$$

Although Equation (118) shows negative correlation except for $\exp(i\pi/4)$, in contrast to the coagulation instability, its physical mechanism is similar to the coagulation instability presented in Section 2. Dust particles are subject to more significant fragmentation in regions of $\delta\Sigma_d > 0$, leading to radial variation of $\delta\tau_s$ and δv_x . The radial gradient of δv_x leads to radial concentration and promotes further fragmentation in the concentrated regions. This positive feedback results in the instability.

The single-size approximation tends to be invalid in the presence of fragmentation and erosion. For comprehensive studies, we should explicitly discuss time evolution of size distribution during the development of the instabilities with fragmentation and erosion, which will be the scope of our future studies.

4.6. Coevolution with Other Dust–Gas Instabilities

Because the coagulation instability is triggered by dust coagulation, the instability is entirely different from any other dust–gas instabilities, including streaming instability (e.g., Youdin & Goodman 2005; Youdin & Johansen 2007; Jacquet et al. 2011), resonant drag instability (Squire & Hopkins 2018a, 2018b), secular GI (e.g., Youdin 2005, 2011; Takahashi & Inutsuka 2014; Tominaga et al. 2019), and TVGI (Tominaga et al. 2019). This is confirmed by taking the limit of $t_0 \rightarrow \infty$ with Equation (13), which leads to $\text{Re}[n_{\text{ap},+}] \rightarrow 0$.

Previous studies on dust collisional growth showed dust depletion when dust grains are spherical and grow into larger sizes ($\tau_s \sim 0.1$) (e.g., Brauer et al. 2008; Okuzumi et al. 2012). The coagulation instability can grow even when dust-to-gas surface density ratio is 10^{-3} while streaming instability, secular GI, and TVGI grow insufficiently in such a dust-poor region. Development of the coagulation instability leads to dust concentration at a small scale $\sim k^{-1}$. Nonlinear development will result in a significant increase in dust surface density by an order of magnitude. If such a nonlinear development is achieved, the coagulation timescale becomes short and collisional growth toward planetesimals might be expected.

If nonlinear development of the coagulation instability increases dust-to-gas ratio from 10^{-3} to 0.02 or even higher, streaming instability subsequently operates in the resultant dust-rich region. Recent studies show that streaming instability can be substantially stabilized if dust particles have a power-law size distribution (Krapp et al. 2019; Paardekooper et al. 2020, 2021;

McNally et al. 2021; Zhu & Yang 2021). McNally et al. (2021) show that adding a bump at the high-mass end of the power-law size distribution makes the stabilization less efficient. Therefore, it is important to study how coagulation instability affects dust size distributions, which will be explored in future work.

If the above dust enrichment and size growth occur in a radially wide region ($\sim H$), we can also expect growth of secular GI and TVGI. Those secular instabilities lead to further dust enrichment at a scale $\lesssim H$, and eventually result in gravitational fragmentation of enriched regions and planetesimal formation (Tominaga et al. 2018, 2019, 2020; Pierens 2021). Resultant planetesimals can be the origin of debris disks and Kuiper Belt objects. We will also investigate planetesimal formation via a combination of coagulation instability, secular GI, and TVGI in future work.

5. Conclusions

In this work, we show that collisional growth of drifting dust leads to a new instability operating in a protoplanetary disk. We refer to the new instability as coagulation instability. Coagulation instability grows at short wavelengths ($< H$) in the absence of dust diffusion, and its growth timescale is much shorter than the coagulation timescale determined by the dust-to-gas mass ratio (Figure 6). Even in the presence of dust diffusion, coagulation instability can grow at a wavelength of $\sim H$ within a few tens of the orbital periods (Figure 8). Although previous studies showed that dust surface density decreases as dust grows, coagulation instability can grow even in a dust-depleted region ($\varepsilon \sim 10^{-3}$) and locally increases dust abundance. Therefore, coagulation instability provides preferable sites for other dust–gas instabilities that require high dust abundance of large dust particles (e.g., $\tau_s \sim 0.1$). In other words, coagulation instability plays an important role for connecting collisional dust growth and hydrodynamical clumping at the early evolutionary stage of protoplanetary disks.

In the present study, we consider time evolution of only the single moment m_p , although we roughly consider the size dispersion by following the formalism proposed by Sato et al. (2016). Considering higher moments and/or evolution of dust size distribution is of significant importance to discussions of whether coagulation instability is viable in protoplanetary disk or not. Those effects will be important at the nonlinear growth phase before the onset of other dust–gas instabilities (e.g., secular GI). Besides, the present analyses are based on the vertically averaged equations and thus neglect vertical shear and stratification. To investigate coagulation instability with vertical direction will be important for discussing its viability in realistic disks (see Appendix C). Our future work will address these issues.

We thank the anonymous referee for the detailed review, which helped to improve the manuscript. We also thank Hidekazu Tanaka, Takeru K. Suzuki, and Sanemichi Z. Takahashi for fruitful discussions. This work was supported by JSPS KAKENHI Grant Nos. JP18J20360 (R.T.T.), 16H02160, 18H05436, 18H05437 (S.I.), 17H01103, 17K05632, 17H01105, 18H05438, 18H05436 and 20H04612 (H.K.). R.T.T. is also supported by RIKEN Special Postdoctoral Researchers Program.

Software: Mathematica (Wolfram Research, Inc 2019), Matplotlib (Hunter 2007), SciPy (Virtanen et al. 2020), NumPy (Harris et al. 2020).

Appendix A Review of Derivation of the Moment Equations and Validity for Coagulation Instability

The moment equation for dust coagulation we adopted was derived in Sato et al. (2016) from the vertically integrated Smoluchowski equation (see also Taki et al. 2021). In this appendix, we review the derivation and mention its validity for the analysis of coagulation instability. We refer readers to Sato et al. (2016) for numerical validation based on comparison with full-size simulations.

In the case of perfect sticking, time evolution of a column number density $N(r, m)$ per unit dust particle mass m is governed by the Smoluchowski equation (Smoluchowski 1916; Schumann 1940; Safronov 1972):

$$\begin{aligned} \frac{\partial mN}{\partial t} = & \frac{m}{2} \int_0^m dm' K(r, m', m - m') \\ & \times N(r, m')N(r, m - m') \\ & - mN(r, m) \int_0^\infty dm' K(r, m, m')N(r, m') \\ & - \frac{1}{r} \frac{\partial}{\partial r} (rv_r(r, m)mN(r, m)), \end{aligned} \quad (\text{A1})$$

where $K(r, m_1, m_2)$ represents collision rates of dust particles with masses of $m_1 = 4\pi\rho_{\text{int}}a_1^3/3$ and $m_2 = 4\pi\rho_{\text{int}}a_2^3/3$. The expression of the collision kernel is given as follows (e.g., Brauer et al. 2008; Okuzumi et al. 2012)

$$\begin{aligned} K(r, m_1, m_2) \equiv & \frac{\sigma_{\text{coll}}}{2\pi H_d(m_1)H_d(m_2)} \int_{-\infty}^{\infty} \Delta v_{\text{pp}} \exp \\ & \times \left[-\frac{z^2}{2} \left(\frac{1}{H_d(m_1)^2} + \frac{1}{H_d(m_2)^2} \right) \right] dz, \end{aligned} \quad (\text{A2})$$

where Δv_{pp} is collision velocity and σ_{coll} is a collisional cross section:

$$\sigma_{\text{coll}} \equiv \pi(a_1 + a_2)^2. \quad (\text{A3})$$

We note that the radial velocity v_r and the dust scale height H_d depend on dust particle mass. Describing coagulation in terms of a column density is valid when vertical mixing of dust particles is faster than coagulation. The timescale of the vertical mixing is on the order of $H_d^2/D \simeq \Omega^{-1}/\tau_s$ (see also Youdin & Lithwick 2007). As mentioned in Section 2, the coagulation timescale is $3t_0/\varepsilon \simeq 1.5\Omega^{-1}/\varepsilon$. The mixing is thus faster than coagulation when dust sizes are large enough ($\tau_s \sim 0.1$) and/or dust-to-gas ratio is decreased ($\varepsilon \sim 10^{-3}$). Such a situation is preferable for coagulation instability. According to Section 4, the growth rate of the instability in the presence of diffusion is $\sim 1 \times 10^{-3}\Omega - 3 \times 10^{-3}\Omega$ for $\tau_{s,0} \simeq 0.1$ and $\varepsilon \simeq 10^{-3}$ (e.g., see Figure 8). Thus, the growth timescale is $\sim 10^2\text{--}10^3\Omega^{-1}$, which is longer than the mixing timescale. This validates our methodology.

Following Sato et al. (2016), we define the i th moment $M_i(r)$

$$M_i(r) \equiv \int_0^\infty m^{i+1}N(r, m)dm. \quad (\text{A4})$$

Using Equations (A1) and (A4), one obtains the i th moment equation (see Estrada & Cuzzi 2008; Ormel & Spaans 2008):

$$\begin{aligned} \frac{\partial M_i}{\partial t} = & \frac{1}{2} \int_0^\infty dm \int_0^\infty dm' K(r, m, m')N(m)N(m') \\ & \times [(m + m')^{i+1} - (m^{i+1} + m'^{i+1})] \\ & - \frac{1}{r} \frac{\partial}{\partial r} (r \langle m^i v_r \rangle_m \Sigma_d), \end{aligned} \quad (\text{A5})$$

where $\langle m^i v_r \rangle_m$ is defined as follows

$$\langle m^i v_r \rangle_m \equiv \frac{1}{\Sigma_d} \int_0^\infty m^{i+1} v_r(m)N(r, m)dm. \quad (\text{A6})$$

One obtains the continuity equation from the zeroth-moment equation

$$\frac{\partial \Sigma_d}{\partial t} + \frac{1}{r} \frac{\partial}{\partial r} (r \langle v_r \rangle_m \Sigma_d) = 0. \quad (\text{A7})$$

The first-moment equation yields

$$\begin{aligned} \frac{\partial m_p \Sigma_d}{\partial t} = & \int_0^\infty dm \int_0^\infty dm' mm' K(r, m, m') \\ & \times N(m)N(m') - \frac{1}{r} \frac{\partial}{\partial r} (r \langle m v_r \rangle_m \Sigma_d), \end{aligned} \quad (\text{A8})$$

where $m_p \equiv M_1/\Sigma_d$ is the weighted average mass, called the peak mass (Ormel & Spaans 2008).

One needs closure relations to solve zeroth- and first-moment equations. Following Sato et al. (2016) and Taki et al. (2021), we assume the following closure relation to approximate $\langle m v_r \rangle_m$ in terms of $v_r(m_p)$:

$$\langle m v_r \rangle_m \simeq m_p \langle v_r \rangle_m \simeq m_p v_r(m_p). \quad (\text{A9})$$

We note that Equation (A9) is more general than the single-size approximation where one explicitly assumes the delta function for dust size distribution. In addition, we further approximate the integral on the right-hand side of Equation (A8). Sato et al. (2016) found that the moment equations reproduce full-size simulations when one approximates the integral by the equal-sized kernel

$$\begin{aligned} & \int_0^\infty dm \int_0^\infty dm' mm' K(r, m, m')N(m)N(m') \\ & \simeq K(m_p, m_p) = \frac{2a^2}{H_d(m_p)} \int_{-\infty}^{\infty} \Delta v_{\text{pp}} \\ & \times \exp\left(-\frac{z^2}{H_d(m_p)^2}\right) dz, \end{aligned} \quad (\text{A10})$$

where we use $m_p = 4\pi\rho_{\text{int}}a^3/3$. Sato et al. (2016) further approximated the vertical integration taking Δv_{pp} outside the integral and obtained

$$K(m_p, m_p) = \frac{2\sqrt{\pi}a^2\Delta v_{\text{pp}}}{H_d(m_p)}. \quad (\text{A11})$$

They showed that using a collision speed Δv_{pp} of dust particles of size ratio 0.5 shows better agreement between full-size simulations and simulations that consider evolution of only Σ_d and m_p (see Appendix A therein). It should be noted that the choice of the size ratio for Δv_{pp} is not so important for $t_{\text{stop}}\Omega \sim 0.1 - 1$, with which the present analysis is concerned.

For example, the turbulence-driven collision velocity that we consider in the main analyses is $\simeq \sqrt{2.3\alpha t_{\text{stop}}\Omega} c_s$ for the size ratio of 0.5 and $\simeq \sqrt{1.9\alpha t_{\text{stop}}\Omega} c_s$ for the size ratio of 1 (Ormel & Cuzzi 2007). The mass distribution is characterized by m_p until the onset of runaway growth (Kobayashi et al. 2016). As the first analysis of coagulation instability, we follow Sato et al. (2016) and only consider the evolution of Σ_d and m_p with Equation (A11). Equations (A7), (A8), (A9), and (A11) give the following equations:

$$\frac{\partial \Sigma_d}{\partial t} + \frac{1}{r} \frac{\partial}{\partial r} (rv_r \Sigma_d) = 0, \quad (\text{A12})$$

$$\frac{dm_p}{dt} = \frac{\partial m_p}{\partial t} + v_r \frac{\partial m_p}{\partial r} = \frac{2\sqrt{\pi} a^2 \Delta v_{\text{pp}} \Sigma_d}{H_d}. \quad (\text{A13})$$

One can derive Equations (1) and (4) adopting the local Cartesian coordinates for these equations.

In the presence of dust diffusion, we should add the diffusion term in the Smoluchowski equation as follows

$$\begin{aligned} \frac{\partial mN}{\partial t} &= \frac{m}{2} \int_0^m dm' K(r, m', m - m') N(r, m') N(r, m - m') \\ &\quad - mN(r, m) \int_0^\infty dm' K(r, m, m') N(r, m') \\ &\quad - \frac{1}{r} \frac{\partial}{\partial r} (rv_r(r, m) mN(r, m)) \\ &\quad + \frac{1}{r} \frac{\partial}{\partial r} \left(rD(r, m) \frac{\partial mN(r, m)}{\partial r} \right), \end{aligned} \quad (\text{A14})$$

where $D(r, m)$ is the diffusion coefficient of dust with a size of m . Here, we only consider the case that diffusion flux is proportional to $\partial N / \partial r$.¹⁰ When we take the moment of Equation (A14), we assume the following relation:

$$\int_0^\infty dm D(r, m) \frac{\partial mN(r, m)}{\partial r} \simeq D(r, m_p) \frac{\partial \Sigma_d}{\partial r}, \quad (\text{A15})$$

$$\int_0^\infty dm D(r, m) m \frac{\partial mN(r, m)}{\partial r} \simeq D(r, m_p) m_p \frac{\partial \Sigma_d}{\partial r}. \quad (\text{A16})$$

This assumption stems from the fact that m_p is the mass-dominating dust size and the mass flux due to the diffusion should be dominated by the mass flux of the mass-dominating dust. The moment equations with the above relations give the equations used in Section 1 once one adopts the local Cartesian coordinates.

Appendix B

Unperturbed State for Two-fluid Analyses without an External Force

In this appendix, we describe the derivation of the unperturbed state adopted in Section 3. The gas surface density and the pressure are assumed to have nonzero but small gradients: $\Sigma'_{g,0}$, $(c_s^2 \Sigma_{g,0})'$. We assume $|x|/R < \Delta R/R \ll 1$ so that we can approximate the unperturbed quantities as constants or linear functions of x :

$$u_x = u_{x,0} + u'_{x,0} x, \quad (\text{B17})$$

¹⁰ To derive the equations in which the diffusion mass flux is proportional to $\partial(\Sigma_d/\Sigma_g)/\partial r$, one has to replace $\partial(m_p N)/\partial r$ with $\Sigma_g \partial(m_p N/\Sigma_g)/\partial r$ in Equation (A14).

$$u_y = -\frac{3}{2}\Omega x + u_{y,0} + u'_{y,0} x, \quad (\text{B18})$$

$$\Sigma_d = \Sigma_{d,0} + \Sigma'_{d,0} x, \quad (\text{B19})$$

$$v_x = v_{x,0} + v'_{x,0} x, \quad (\text{B20})$$

$$v_y = -\frac{3}{2}\Omega x + v_{y,0} + v'_{y,0} x, \quad (\text{B21})$$

$$\tau_s = \tau_{s,0} + \tau'_{s,0} x. \quad (\text{B22})$$

We also assume that the pressure $c_s^2 \Sigma_g$ is a smooth function in x and can be approximated as a linear function, i.e., $c_s^2 \Sigma_g = c_s^2 \Sigma_{g,0} + (c_s^2 \Sigma_{g,0})' x$. The temperature structure is assumed in the present analyses. Thus, we have 12 variables to determine the unperturbed state.

To analytically solve the set of 12 equations (Equations(35)–(40)) is difficult. To approximately derive unperturbed state values, we first make use of the assumption that spatial gradients of the gas pressure and density ($(c_s^2 \Sigma_{g,0})'$, $\Sigma'_{g,0}$) are so small that second- and higher-order terms of those gradients can be neglected. This assumption is valid for the following cases: (1) those gradients originate from a global disk profile without a small-scale characteristic structure (e.g., a pressure bump), i.e., $\Sigma'_{g,0} x / \Sigma_{g,0} \sim (c_s^2 \Sigma_{g,0})' x / (c_s^2 \Sigma_{g,0}) \sim x/R$, and (2) the local domain with a width of ΔR satisfies $x \ll \Delta R \ll R$. Considering given gas profiles, Σ_g , $c_s^2 \Sigma_g$, with such small gradients, we seek a drift solution that requires the velocities, $u_{x,0}$, $u_{y,0}$, $v_{x,0}$, and $v_{y,0}$, to be linearly proportional to the gas pressure gradient $(c_s^2 \Sigma_g)' = (c_s^2 \Sigma_{g,0})'$. In other words, those velocities are already of the first order in $(c_s^2 \Sigma_{g,0})'$ and $\Sigma'_{g,0}$ because of the nature of the drift, which one should keep in mind below. We also assume that the spatial gradients of the other variables (e.g., $\Sigma'_{d,0}$) are small and satisfy $A'x/A \sim x/R \ll 1$, where $A = \{\Sigma_{d,0}, u_{x,0}, v_{x,0}, u_{y,0}, v_{y,0}, \tau_{s,0}\}$. Based on those assumptions, we derive an approximated steady drift solution that is valid at the first order in the gradients, i.e., $\mathcal{O}(x/R)$, by neglecting the higher-order terms.

First, the continuity equation for gas (Equation (35)) gives

$$\Sigma'_{g,0} u_{x,0} + \Sigma_{g,0} u'_{x,0} + 2\Sigma'_{g,0} u'_{x,0} x = 0. \quad (\text{B23})$$

Equation (B23) is satisfied for arbitrary x when the coefficients of the polynomial of x are zero at the first order in x/R :

$$\Sigma'_{g,0} u_{x,0} + \Sigma_{g,0} u'_{x,0} = \mathcal{O}((x/R)^2), \quad (\text{B24})$$

$$\Sigma'_{g,0} u'_{x,0} = \mathcal{O}((x/R)^2). \quad (\text{B25})$$

As noted above, $u_{x,0}$ is the first order in $(c_s^2 \Sigma_{g,0})'$ for the drift solution. Therefore, the first term in Equation (B24) is the second order. For Equation (B24) to be satisfied at the first order in the gradients, the spatial derivative of u_x should be zero, or more precisely, the higher order in the gradients. This is reasonable for the drift solution because the spatial derivative of $u_{x,0}$ will introduce combinations of $(c_s^2 \Sigma_{g,0})'$ and the first-order gradient of other variables, meaning that $u'_{x,0}$ is the higher-order term. Therefore, as long as we consider the drift solution, the left-hand side of Equation (B24) includes only the higher-order terms of the gradients, and the equality is automatically satisfied. One then finds that Equation (B25) is also satisfied because $\Sigma'_{g,0} u'_{x,0}$ is the third-order for the drift solution. For simplicity, we set $u'_{x,0} = 0$ in the following,

which is justified as long as we conduct analyses that are valid at the first order in x/R . In the same way, one finds that the continuity equation for dust (Equation (38)) is also satisfied at the first order for the drift solution we seek. For example, we have $\Sigma'_{d,0} v_{x,0} \sim \mathcal{O}((x/R)^2)$. We set $v'_{x,0} = 0$ for simplicity as in the case of $u'_{x,0}$. This choice is valid in the present analyses of the first order of x/R .

Equations (36), (37), (39), and (40) generally introduce eight equations to determine the unperturbed state from the coefficients of the polynomial of x , i.e., x^0 and x^1 . One can freely fix four variables because the number of variables is larger than the number of equations. In the present analyses, we regard $\Sigma_{d,0}$ and $\tau_{s,0}$ as input parameters and set $\Sigma'_{d,0} = \tau'_{s,0} = 0$. The dust surface density gradient can be safely neglected in a steady state that is valid at the first order in x/R . This is because the dust continuity equation is automatically satisfied as long as we consider the drift solution with the small gradients, which includes $\Sigma'_{d,0}$ (see the above discussion). The assumption of $\tau'_{s,0} = 0$ mimics the drift-limited coagulation, where the dimensionless stopping time tends to be uniform (e.g., see Okuzumi et al. 2012). For the drift solution we seek, the spatial derivative of $\tau_{s,0}$ only appears in the equations when we keep terms of the higher order in the gradients, and thus we safely neglect $\tau'_{s,0}$ in the first-order analyses. In this case, we find the following velocity fields from the equations of motion:

$$u_{x,0} = \frac{2\varepsilon\tau_{s,0}}{(1+\varepsilon)^2 + \tau_{s,0}^2} \left(-\frac{(c_s^2 \Sigma_{g,0})'}{2\Omega \Sigma_{g,0}} \right), \quad (\text{B26})$$

$$u_{y,0} = - \left[1 + \frac{\varepsilon\tau_{s,0}^2}{(1+\varepsilon)^2 + \tau_{s,0}^2} \right] \left(-\frac{(c_s^2 \Sigma_{g,0})'}{2\Omega \Sigma_{g,0}(1+\varepsilon)} \right), \quad (\text{B27})$$

$$v_{x,0} = -\frac{2\tau_{s,0}}{(1+\varepsilon)^2 + \tau_{s,0}^2} \left(-\frac{(c_s^2 \Sigma_{g,0})'}{2\Omega \Sigma_{g,0}} \right), \quad (\text{B28})$$

$$v_{y,0} = - \left[1 - \frac{\tau_{s,0}^2}{(1+\varepsilon)^2 + \tau_{s,0}^2} \right] \left(-\frac{(c_s^2 \Sigma_{g,0})'}{2\Omega \Sigma_{g,0}(1+\varepsilon)} \right), \quad (\text{B29})$$

and $v_{y,0}' = u_{y,0}' = 0$ at the first order of x/R . These are the unperturbed velocity fields presented in Section 3. In this way, instead of invoking an external force, we find a simple solution valid at the first order of x/R for the unperturbed state with finite drift velocities where x -dependence appears only in the gas surface density and pressure.

Appendix C

Sublayer Model with Uniform Surface Densities

In Section 3, we perform two-fluid linear analyses with vertically full averaging despite the large difference in vertical scale heights of dust and gas disks. On the other hand, when vertical momentum mixing/transfer in the gas disk is weak, the dust–gas momentum exchange should be averaged within a dust–gas sublayer. Such a sublayer modeling is invoked in some two-fluid linear analyses on dust–gas instabilities (e.g., Latter & Rosca 2017). In this appendix, we consider such a limiting case of weak momentum mixing in gas and discuss its effect on coagulation instability. We find that sublayer analyses show insignificant difference, and results can be reproduced

well by the one-fluid dispersion relation as long as the total dust-to-gas ratio ε is smaller than 10^{-2} .

In the sublayer model, we divide a gas disk into a sublayer gas and an upper gas that is steady and not perturbed. We denote a surface density of the sublayer gas by $\Sigma_{g,s}$. A surface density of the upper steady gas is given by $\Delta\Sigma_g \equiv \Sigma_g - \Sigma_{g,s}$. Vertical boundary positions of the sublayer are denoted by $z = \pm z_s$. Thus, for a stratified gas disk, the sublayer-gas surface density is given as follows

$$\Sigma_{g,s} = \Sigma_g \operatorname{erf} \left[\frac{z_s}{\sqrt{2H}} \right]. \quad (\text{C1})$$

We adopt $z_s \geq 3H_d$ so that most of the dust grains are included in the sublayer. For simplicity, we equate a sublayer-dust surface density $\Sigma_{d,s}$ to the dust surface density Σ_d . Larger z_s means that Reynolds stress (or Maxwell stress in a magnetized disk) transfer momentum to higher altitude, and momentum exchange is effectively balanced between dust and a larger amount of gas. We neglect momentum transport between sublayer gas and upper gas in order to make analyses as simple as possible. The setup is summarized in Figure 14.

We assume that z_s is constant in time and space and determined by the unperturbed value of dimensionless stopping time $\tau_{s,0}$. This assumption excludes the effect of the τ_s -dependent midplane dust–gas ratio adopted in Section 4.2, which enables us to focus on an effect of sublayer-gas motion on the present instability.

To avoid further complexity, we follow the widely adopted formalism that we add an external force on gas to set up dust–gas drift motion in the unperturbed state (e.g., Youdin & Goodman 2005; Youdin & Johansen 2007). The sublayer-gas equations are the following:

$$\frac{\partial \Sigma_{g,s}}{\partial t} + \frac{\partial \Sigma_{g,s} u_x}{\partial x} = 0, \quad (\text{C2})$$

$$\begin{aligned} \frac{\partial u_x}{\partial t} + u_x \frac{\partial u_x}{\partial x} &= 3\Omega^2 x + 2\Omega u_y + 2\eta R \Omega^2 \\ &- \frac{c_s^2}{\Sigma_{g,s}} \frac{\partial \Sigma_{g,s}}{\partial x} + \frac{\Sigma_d}{\Sigma_{g,s}} \frac{v_x - u_x}{\tau_s} \Omega, \end{aligned} \quad (\text{C3})$$

$$\frac{\partial u_y}{\partial t} + u_x \frac{\partial u_y}{\partial x} = -2\Omega u_x + \frac{\Sigma_d}{\Sigma_{g,s}} \frac{v_y - u_y}{\tau_s} \Omega, \quad (\text{C4})$$

$$\frac{\partial \Delta \Sigma_g}{\partial t} = \frac{\partial \Delta \Sigma_g}{\partial x} = 0, \quad (\text{C5})$$

where the third term on the right-hand side of Equation (C3) is the external force introduced in the previous studies. For dust equations, we use Equations (31), (32), and (33). The moment equation for dust coagulation is

$$\begin{aligned} \frac{\partial \tau_s}{\partial t} + v_x \frac{\partial \tau_s}{\partial x} &= \frac{\Sigma_d}{\Sigma_g} \frac{\tau_s}{3t_0} \\ &+ \frac{\tau_s}{\Sigma_g} \frac{\partial \Sigma_{g,s} u_x}{\partial x} - \frac{\tau_s}{\Sigma_g} v_x \frac{\partial \Sigma_g}{\partial x}. \end{aligned} \quad (\text{C6})$$

This equation can be derived from Equations (4), (7), (C2), and (C5). We note that coagulation rate is determined by Σ_g/Σ_g even in the sublayer model.

With the aid of the external force in Equation (C3), we adopt an unperturbed state with uniform surface densities $\Sigma_{g,0}$, $\Sigma_{d,0}$,

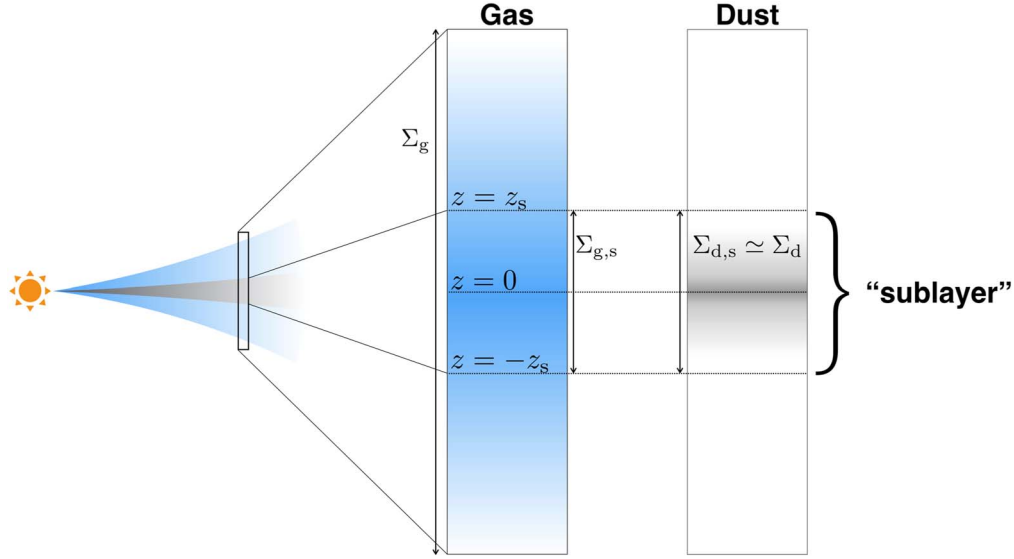


Figure 14. Schematic picture of setups in the sublayer model. We assume the upper gas at $|z| > z_s$ to be steady and that dust and gas within the sublayer ($|z| \leq z_s$) evolve during the development of coagulation instability.

and $\Sigma_{g,s,0}$. In the current sublayer model, we exclude the stabilizing effect from the unperturbed surface density profile, i.e., the last term of Equation (C6), because the term is the same as the term in the full-disk-averaging equation and its effect is already discussed in Section 3. The unperturbed velocities are given by the usual drift solution (e.g., Nakagawa et al. 1986):

$$u_x = u_{x,0} = \frac{2(\Sigma_{d,0}/\Sigma_{g,s,0})\tau_{s,0}}{(1 + \Sigma_{d,0}/\Sigma_{g,s,0})^2 + \tau_{s,0}^2} \eta R \Omega, \quad (\text{C7})$$

$$u_y = -\frac{3}{2} \Omega x + u_{y,0}, \quad (\text{C8})$$

$$u_{y,0} = -\left[1 + \frac{(\Sigma_{d,0}/\Sigma_{g,s,0})\tau_{s,0}^2}{(1 + \Sigma_{d,0}/\Sigma_{g,s,0})^2 + \tau_{s,0}^2} \right] \frac{\eta R \Omega}{1 + \Sigma_{d,0}/\Sigma_{g,s,0}}, \quad (\text{C9})$$

$$v_{x,0} = -\frac{2\tau_{s,0}}{(1 + \Sigma_{d,0}/\Sigma_{g,s,0})^2 + \tau_{s,0}^2} \eta R \Omega, \quad (\text{C10})$$

$$v_y = -\frac{3}{2} \Omega x + v_{y,0}, \quad (\text{C11})$$

$$v_{y,0} = -\left[1 - \frac{\tau_{s,0}^2}{(1 + \Sigma_{d,0}/\Sigma_{g,s,0})^2 + \tau_{s,0}^2} \right] \frac{\eta R \Omega}{1 + \Sigma_{d,0}/\Sigma_{g,s,0}}, \quad (\text{C12})$$

As in Section 3, we adopt a value of η obtained for the MMSN disk model and $R = 20$ au. We note that the drift velocities are related to the dust–gas ratio averaged in the sublayer: $\Sigma_{d,0}/\Sigma_{g,s,0}$, which is in contrast to the analyses in Section 3. Based on the above unperturbed state value, we linearize Equations (31), (32), (33), (C2), (C3), (C4), and (C6) and derive growth rates $n = n_{2\text{fsub}}$ of coagulation instability. We also assume $\delta\Sigma_{g,s} = \delta\Sigma_g$ based on the assumption of the steady upper gas (Equation (C5)).

An upper panel of Figure 15 shows the growth rates $n_{2\text{fsub}}$ for $z_s = 3H_d$, $10H_d$ with the other parameter being fixed:

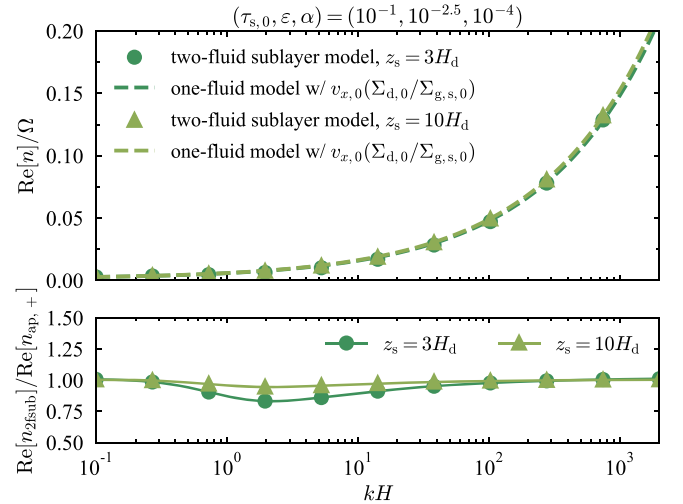


Figure 15. The upper panel shows growth rates for $z_s = 3H_d$, $10H_d$ and compares the obtained growth rates with the one-fluid growth rates $n_{\text{ap},+}$. We find that the growth rate in the sublayer model can be reproduced well by $n_{\text{ap},+}$. The lower panel shows the ratio of the two growth rates. The ratio has its minimum at $kH \simeq 2$. We find that the difference from the one-fluid growth rate is only a few tens of percent for $z_s = 3H_d$ and less for $z_s = 10H_d$.

$(\tau_{s,0}, \varepsilon, \alpha) = (10^{-1}, 10^{-2.5}, 10^{-4})$. We also plot one-fluid growth rate $n_{\text{ap},+}$ (Equation (13)) but we substitute the modified unperturbed drift velocity (Equation (C10)) in the one-fluid dispersion relation. The growth rates in the two-fluid sublayer model are reproduced well by the one-fluid growth rates. Besides, based on the discussion in Section 3, this also indicates that the sublayer analyses and the full-disk analyses give essentially the same results, and differences are mainly from (1) different drift velocity and (2) the effect of the unperturbed gas density profile (the last term of Equation (C6)). The lower panel of Figure 15 shows the ratio $\text{Re}[n_{2\text{fsub}}]/\text{Re}[n_{\text{ap},+}]$ as a function of kH . The difference of the two growth rates is at its maximum at $kH \simeq 2$. Nevertheless, the difference from the one-fluid growth rate is only a few tens

of percent for $z_s = 3H_d$ and less for $z_s = 10H_d$. The difference monotonically decreases with increasing z_s .

We find that the difference between $\text{Re}[n_{2\text{fsub}}]$ and $\text{Re}[n_{\text{ap},+}]$ for other parameters is also maximum at $kH \simeq 1 - 10$ (e.g., $\alpha = 10^{-5}$). The difference from one-fluid growth rates is still about a few tens of percent to about 50% even for $\alpha = 10^{-5}$ when total dust-to-gas ratio is 10^{-3} and $\tau_{s,0} = 10^{-1}$, which are realistic values based on the previous dust growth simulations with the MMSN model (e.g., see Section 3.1 of Okuzumi et al. 2012). Therefore, coagulation instability and resulting dust reaccumulation in dust-depleted regions are viable even when the momentum mixing in the gas disk is weak.

ORCID iDs

Ryosuke T. Tominaga  <https://orcid.org/0000-0002-8596-3505>
 Shu-ichiro Inutsuka  <https://orcid.org/0000-0003-4366-6518>
 Hiroshi Kobayashi  <https://orcid.org/0000-0001-8808-2132>

References

- Abod, C. P., Simon, J. B., Li, R., et al. 2019, *ApJ*, 883, 192
 Adachi, I., Hayashi, C., & Nakazawa, K. 1976, *PTHPh*, 56, 1756
 Auffinger, J., & Laibe, G. 2018, *MNRAS*, 473, 796
 Bai, X.-N., & Stone, J. M. 2010, *ApJL*, 722, L220
 Bai, X.-N., & Stone, J. M. 2014, *ApJ*, 796, 31
 Barge, P., & Sommeria, J. 1995, *A&A*, 295, L1
 Birnstiel, T., Dullemond, C. P., & Brauer, F. 2009, *A&A*, 503, L5
 Birnstiel, T., Klahr, H., & Ercolano, B. 2012, *A&A*, 539, A148
 Brauer, F., Dullemond, C. P., & Henning, T. 2008, *A&A*, 480, 859
 Carballido, A., Fromang, S., & Papaloizou, J. 2006, *MNRAS*, 373, 1633
 Carrera, D., Johansen, A., & Davies, M. B. 2015, *A&A*, 579, A43
 Carrera, D., Simon, J. B., Li, R., Kretke, K. A., & Klahr, H. 2021, *AJ*, 161, 96
 Casassus, S., Wright, C. M., Marino, S., et al. 2015, *ApJ*, 812, 126
 Chavanis, P. H. 2000, *A&A*, 356, 1089
 Chen, K., & Lin, M.-K. 2020, *ApJ*, 891, 132
 Cuzzi, J. N., Dobrovolskis, A. R., & Champney, J. M. 1993, *Icar*, 106, 102
 Drążkowska, J., & Alibert, Y. 2017, *A&A*, 608, A92
 Drążkowska, J., & Dullemond, C. P. 2014, *A&A*, 572, A78
 Dubrulle, B., Morfill, G., & Sterzik, M. 1995, *Icar*, 114, 237
 Dzyurkevich, N., Flock, M., Turner, N. J., Klahr, H., & Henning, T. 2010, *A&A*, 515, A70
 Estrada, P. R., & Cuzzi, J. N. 2008, *ApJ*, 682, 515
 Flock, M., Ruge, J. P., Dzyurkevich, N., et al. 2015, *A&A*, 574, A68
 Fukagawa, M., Tsukagoshi, T., Momose, M., et al. 2013, *PASJ*, 65, L14
 Gerbig, K., Murray-Clay, R. A., Klahr, H., & Baehr, H. 2020, *ApJ*, 895, 91
 Goldreich, P., & Lynden-Bell, D. 1965, *MNRAS*, 130, 125
 Gole, D. A., Simon, J. B., Li, R., Youdin, A. N., & Armitage, P. J. 2020, *ApJ*, 904, 132
 Gonzalez, J. F., Laibe, G., & Maddison, S. T. 2017, *MNRAS*, 467, 1984
 Goodman, J., & Pindor, B. 2000, *Icar*, 148, 537
 Harris, C. R., Millman, K. J., van der Walt, S. J., et al. 2020, *Natur*, 585, 357
 Hayashi, C. 1981, *PTHPS*, 70, 35
 Hunter, J. D. 2007, *CSE*, 9, 90
 Jacquet, E., Balbus, S., & Latter, H. 2011, *MNRAS*, 415, 3591
 Johansen, A., Oishi, J. S., Mac Low, M.-M., et al. 2007, *Natur*, 448, 1022
 Johansen, A., Youdin, A., & Klahr, H. 2009a, *ApJ*, 697, 1269
 Johansen, A., Youdin, A., & Mac Low, M.-M. 2009b, *ApJL*, 704, L75
 Kataoka, A., Tanaka, H., Okuzumi, S., & Wada, K. 2013a, *A&A*, 557, L4
 Kataoka, A., Tanaka, H., Okuzumi, S., & Wada, K. 2013b, *A&A*, 554, A4
 Kimura, H., Wada, K., Senshu, H., & Kobayashi, H. 2015, *ApJ*, 812, 67
 Kobayashi, H., Tanaka, H., & Okuzumi, S. 2016, *ApJ*, 817, 105
 Krapp, L., Benítez-Llambay, P., Gressel, O., & Pessah, M. E. 2019, *ApJL*, 878, L30
 Kretke, K. A., & Lin, D. N. C. 2007, *ApJL*, 664, L55
 Krijt, S., Ormel, C. W., Dominik, C., & Tielens, A. G. G. M. 2015, *A&A*, 574, A83
 Lambrechts, M., Johansen, A., Capelo, H. L., Blum, J., & Bodenschatz, E. 2016, *A&A*, 591, A133
 Latter, H. N., & Rosca, R. 2017, *MNRAS*, 464, 1923
 Lin, M.-K., & Youdin, A. N. 2017, *ApJ*, 849, 129
 Lyra, W., & Lin, M.-K. 2013, *ApJ*, 775, 17
 McNally, C. P., Lovascio, F., & Paardekooper, S.-J. 2021, *MNRAS*, 502, 1469
 Nakagawa, Y., Nakazawa, K., & Hayashi, C. 1981, *Icar*, 45, 517
 Nakagawa, Y., Sekiya, M., & Hayashi, C. 1986, *Icar*, 67, 375
 Okuzumi, S., & Hirose, S. 2012, *ApJL*, 753, L8
 Okuzumi, S., Momose, M., Sirono, S.-i., Kobayashi, H., & Tanaka, H. 2016, *ApJ*, 821, 82
 Okuzumi, S., Tanaka, H., Kobayashi, H., & Wada, K. 2012, *ApJ*, 752, 106
 Ormel, C. W., & Cuzzi, J. N. 2007, *A&A*, 466, 413
 Ormel, C. W., & Spaans, M. 2008, *ApJ*, 684, 1291
 Paardekooper, S.-J., McNally, C. P., & Lovascio, F. 2020, *MNRAS*, 499, 4223
 Paardekooper, S.-J., McNally, C. P., & Lovascio, F. 2021, *MNRAS*, 502, 1579
 Pierens, A. 2021, *MNRAS*, 504, 4522
 Raettig, N., Klahr, H., & Lyra, W. 2015, *ApJ*, 804, 35
 Safronov, V. S. 1972, *Evolution of the Protoplanetary Cloud and Formation of the Earth and Planets* (Jerusalem: Keter Publishing)
 Saito, E., & Sirono, S.-i. 2011, *ApJ*, 728, 20
 Sato, T., Okuzumi, S., & Ida, S. 2016, *A&A*, 589, A15
 Schoonenberg, D., & Ormel, C. W. 2017, *A&A*, 602, A21
 Schoonenberg, D., Ormel, C. W., & Krijt, S. 2018, *A&A*, 620, A134
 Schumann, T. E. W. 1940, *QJRMS*, 66, 195
 Shakura, N. I., & Sunyaev, R. A. 1973, *A&A*, 24, 337
 Shu, F. H. 1992, *The Physics of Astrophysics. Volume II: Gas Dynamics* (Mill Valley, CA (USA): Univ. Science Books)
 Simon, J. B., Armitage, P. J., Li, R., & Youdin, A. N. 2016, *ApJ*, 822, 55
 Smoluchowski, M. V. 1916, *ZPhy*, 17, 557
 Squire, J., & Hopkins, P. F. 2018a, *MNRAS*, 477, 5011
 Squire, J., & Hopkins, P. F. 2018b, *ApJL*, 856, L15
 Steinpilz, T., Teiser, J., & Wurm, G. 2019, *ApJ*, 874, 60
 Stevenson, D. J., & Lunine, J. I. 1988, *Icar*, 75, 146
 Takahashi, S. Z., & Inutsuka, S.-i. 2014, *ApJ*, 794, 55
 Taki, T., Fujimoto, M., & Ida, S. 2016, *A&A*, 591, A86
 Taki, T., Kuwabara, K., Kobayashi, H., & Suzuki, T. K. 2021, *ApJ*, 909, 75
 Tominaga, R. T., Inutsuka, S.-i., & Takahashi, S. Z. 2018, *PASJ*, 70, 3
 Tominaga, R. T., Takahashi, S. Z., & Inutsuka, S.-i. 2019, *ApJ*, 881, 53
 Tominaga, R. T., Takahashi, S. Z., & Inutsuka, S.-i. 2020, *ApJ*, 900, 182
 Ueda, T., Flock, M., & Okuzumi, S. 2019, *ApJ*, 871, 10
 Umurhan, O. M., Estrada, P. R., & Cuzzi, J. N. 2020, *ApJ*, 895, 4
 van der Marel, N., van Dishoeck, E. F., Bruderer, S., et al. 2013, *Sci*, 340, 1199
 Virtanen, P., Gommers, R., Oliphant, T. E., et al. 2020, *NatMe*, 17, 261
 Völk, H. J., Jones, F. C., Morfill, G. E., & Roeser, S. 1980, *A&A*, 85, 316
 Wada, K., Tanaka, H., Okuzumi, S., et al. 2013, *A&A*, 559, A62
 Wada, K., Tanaka, H., Suyama, T., Kimura, H., & Yamamoto, T. 2009, *ApJ*, 702, 1490
 Ward, W. R. 2000, in *On Planetary Formation: The Role of Collective Particle Behavior*, ed. R. M. Canup, K. Righter et al. (Tucson, AZ: Univ. Arizona Press), 75
 Weidenschilling, S. J. 1977, *MNRAS*, 180, 57
 Whipple, F. L. 1972, in *From Plasma to Planet*, ed. A. Elvius (New York: Wiley), 211
 Wolfram Research, Inc 2019, *Mathematica*, v 12.0, <https://www.wolfram.com/mathematica/?source=nav>
 Yang, C. C., Johansen, A., & Carrera, D. 2017, *A&A*, 606, A80
 Youdin, A., & Johansen, A. 2007, *ApJ*, 662, 613
 Youdin, A. N. 2011, *ApJ*, 731, 99
 Youdin, A. N. 2005, arXiv:astro-ph/0508659
 Youdin, A. N., & Goodman, J. 2005, *ApJ*, 620, 459
 Youdin, A. N., & Lithwick, Y. 2007, *Icar*, 192, 588
 Zhu, Z., & Yang, C.-C. 2021, *MNRAS*, 501, 467